Surface Flux Observations on the Southeastern Tropical Pacific Ocean and Attribution of SST Errors in Coupled Ocean–Atmosphere Models

Simon P. de Szoeke

College of Oceanic and Atmospheric Sciences, Oregon State University, Corvallis, Oregon

Christopher W. Fairall and Daniel E. Wolfe

National Oceanic and Atmospheric Administration/Earth System Research Laboratory, Boulder, Colorado

Ludovic Bariteau

Cooperative Institute for Research in the Environmental Sciences, University of Colorado, and National Oceanic and Atmospheric Administration/Earth System Research Laboratory, Boulder, Colorado

Paquita Zuidema

Rosenstiel School of Marine and Atmospheric Science, University of Miami, Miami, Florida

(Manuscript received 4 September 2009, in final form 2 March 2010)

ABSTRACT

A new dataset synthesizes in situ and remote sensing observations from research ships deployed to the southeastern tropical Pacific stratocumulus region for 7 years in boreal fall. Surface meteorology, turbulent and radiative fluxes, aerosols, cloud properties, and rawinsonde profiles were measured on nine ship transects along 20°S from 75° to 85°W. Fluxes at the ocean surface are essential to the equilibrium SST. Solar radiation is the only warming net heat flux, with 180–200 W m^{-2} in boreal fall. The strongest cooling is evaporation (60–100 W m^{-2}), followed by net thermal infrared radiation (30 W m^{-2}) and sensible heat flux ($<$10 W m^{-2}). The 70 W m^{-2} imbalance of heating at the surface reflects the seasonal SST tendency and some 30 W m^{-2} cooling that is mostly due to ocean transport.

Coupled models simulate significant SST errors in the eastern tropical Pacific Ocean. Three different observation-based gridded ocean surface flux products agree with ship and buoy observations, while fluxes simulated by 15 Coupled Model Intercomparison Project phase 3 [CMIP3; used for the Intergovernmental Panel on Climate Change (IPCC) Fourth Assessment Report] general circulation models have relatively large errors. This suggests the gridded observation-based flux datasets are sufficiently accurate for verifying coupled models. Longwave cooling and solar warming are correlated among model simulations, consistent with cloud radiative forcing and low cloud amount differences. In those simulations with excessive solar heating, elevated SST also results in larger evaporation and longwave cooling to compensate for the solar excess. Excessive turbulent heat fluxes (10–90 W m^{-2} cooling, mostly evaporation) are the largest errors in simulations once the compensation between solar and longwave radiation is taken into account. In addition to excessive solar warming and evaporation, models simulate too little oceanic residual cooling in the southeastern tropical Pacific Ocean.

1. Introduction

Southeasterly winds blow over the southeastern tropical Pacific Ocean off the west coast of South America.

The alongshore wind stress drives cold water upwelling at the coast. Figure 1a shows mean sea surface temperature (SST) from the Advanced Microwave Scanning Radiometer for Earth Observing System (AMSR-E climatology of Risien and Chelton 2008) from 30°S to the equator, 70°–100°W computed from June 2002 to October 2009. Cool SST is found to the southeast of the region in Fig. 1 and in a thin 200-km strip along the South American coast. Southeasterly advection of air from

Corresponding author address: Simon P. de Szoeke, College of Oceanic and Atmospheric Sciences, Oregon State University, 104 COAS Admin. Bldg., Corvallis, OR 97331-5503.
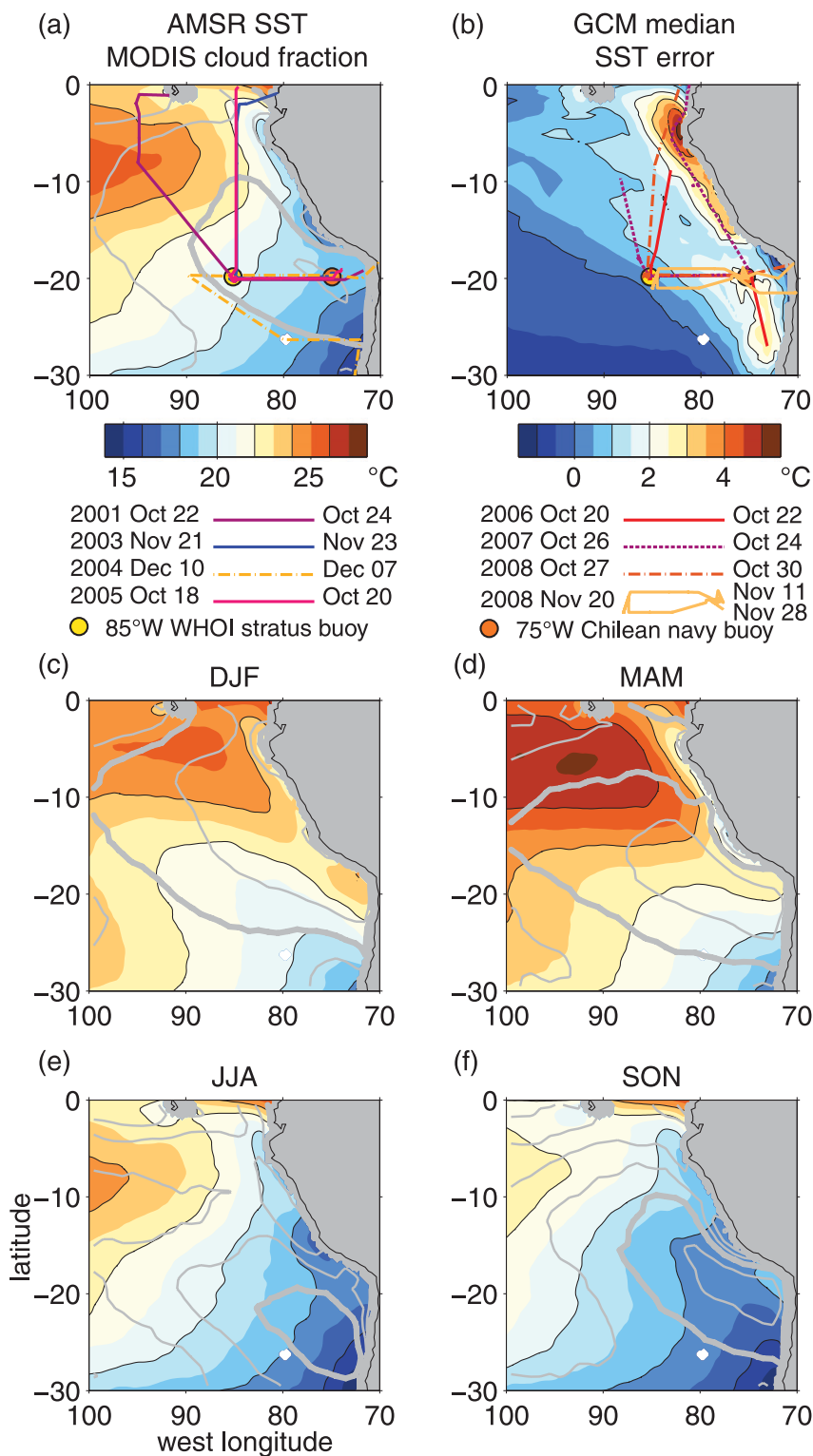E-mail: sdeszoek@coas.oregonstate.edu

FIG. 1. SST (shaded) from AMSR and cloud fraction (gray) from MODIS satellite data: (a) annual mean, (b) median SST error of 15 coupled GCMs in the CMIP3 dataset, (c) December–February 3-month seasonal satellite average, (d) March–May, (e) June–August, and (f) September–November. Ship tracks of the seven stratocumulus cruises in the southeastern tropical Pacific in years 2001–08 are shown in (a),(b). The legend below (a),(b) shows dates when the ship was at (left) 85°W and (right) 75°W for nine 20°S transects. The contour intervals are 2°C for SST, 1°C for SST error, and 10% for cloud fraction. The 80% cloud fraction contour is thickened.

cooler to warmer SST results in positive moisture and buoyancy flux from the ocean surface and a stratocumulus cloud-capped marine atmospheric boundary layer. Cloud fraction for 2001–09 from the Moderate Resolution Imaging Spectroradiometer (MODIS; Platnick et al. 2003) instruments is contoured in Fig. 1a. High-albedo stratocumulus clouds extend widely west of the coast in latitudes 10°–25°S. Cloud fraction mostly increases eastward, but a narrow cloud cover minimum lies over the cool SST within 200 km of the coast. The coolest SST in the seasonal cycle is found in September–November (Fig. 1f). Cloud fraction is expanding in this season and reaches 80% at 20°S, 85°W.

Most coupled ocean–atmosphere models simulate warm SST errors west of the South American coast in the tropical Pacific Ocean. The warm SST error is often attributed to excessive absorption of solar radiation by the ocean because of insufficient simulation of stratiform clouds. Another mechanism suggests that insufficient ocean upwelling and offshore transport of cold water from the South American coast are responsible for the warm error. The median model error (Fig. 1b) from 15 coupled general circulation models (GCMs) from the Coupled Model Intercomparison Project phase 3 (CMIP3) shows the warmest SST errors confined within 500 km of the coast. In addition to the coastal warm error, most models have positive errors extending offshore into the cloud deck. Positive median errors extend to 20°S, 85°W. Warm SST errors in the Southern Hemisphere weaken the north–south asymmetry of SST observed over the eastern tropical Pacific Ocean and contribute to errors in the cross-equatorial wind and seasonal ITCZ precipitation errors (de Szoeke and Xie 2008; Mechoso et al. 1995).

As over most tropical oceans, in the southeastern tropical Pacific, absorption of solar radiation is the largest term in the surface heat budget, warming the ocean surface. Solar warming is only partly compensated by evaporation, thermal infrared radiation, and sensible turbulent heat flux from the ocean surface. Measuring the surface flux components of the heat budget leads to better understanding of the terms influencing the SST, and assessing these terms in models will help us diagnose reasons for SST errors in simulations.

Seven ship cruises from 2001 to 2008 have collected climate-quality time series of surface meteorological observations, extending monitoring during service of the Woods Hole Oceanographic Institution (WHOI) Stratus Ocean Reference Station buoy at 20°S, 85°W (Colbo and Weller 2007). Each cruise made a transect along 20°S from 85° to 75°W in late boreal fall, sampling a section stretching from the cool coastal water, where most models have SST errors greater than 2°C (Fig. 1b),

to 85°W. The route of the ships in the vicinity of the 20°S transect is shown for each year in Figs. 1a and 1b. The dates the ships reached 85° and 75°W each year are printed to the left and right of the legends below the panels, respectively. The research cruises sailed from west to east, except for three transects in 2004, 2007, and 2008. Most cruises were in October; however, the two in 2003 and 2008 were in November and the one in 2004 was in December.

A dataset integrating ship-based surface meteorology, cloud, aerosol, and rawinsonde observations for each of these cruises has been processed into a consistent format for all seven cruises. The dataset is intended for the use of the scientific community for projects such as climate analysis and model assessment. Data from the Eastern Pacific Investigation of Climate (EPIC) stratocumulus cruise of 2001, the first of the stratocumulus cruises in our synthesis dataset, have been used to suggest relations between aerosols, stratocumulus clouds, and drizzle (Bretherton et al. 2004; Comstock et al. 2005). The European Cloud System (EUROCS) project (Siebesma et al. 2004) assessed atmospheric models along a virtual eastern Pacific transect to improve cloud and precipitation simulations. Surface radiative fluxes and cloud forcing were observed on the 1999–2002 Pan American Climate Studies (PACS) cruises in the equatorial eastern Pacific along the 95° and 110°W Tropical Atmosphere Ocean (TAO) buoy lines (Fairall et al. 2008). Colbo and Weller (2007) estimated the contribution of surface fluxes and subsurface ocean processes to the heat budget from data collected by the WHOI Stratus buoy at 20°S, 85°W. Toniazzo et al. (2010) used an eddy-permitting ocean model, and Zheng et al. (2010) used an eddy-resolving ocean model to estimate geostrophic, wind-driven, and eddy contributions to the upper-ocean heat budget. This paper analyzes the eastern tropical Pacific stratocumulus region using ship observations from the synthesis dataset along the repeated 20°S section, with emphasis on the surface fluxes.

New gridded data products interpolate and combine satellite retrievals, reanalysis, and model data of surface quantities to derive surface fluxes over the ocean. These products are useful for assessing air–sea interaction in climate and operational models. We assess climatological averages of several gridded flux products on the 20°S section. On the basis of persistent model errors in the tropical Pacific, we expect 20°S to be a challenging test of the accuracy of flux products.

This paper has several aims. Section 2 introduces a new synthesis dataset of observations made from ships in the southeastern tropical Pacific. The appendix documents the ship observations and the methods for integrating them into a unified synthesis dataset. We also
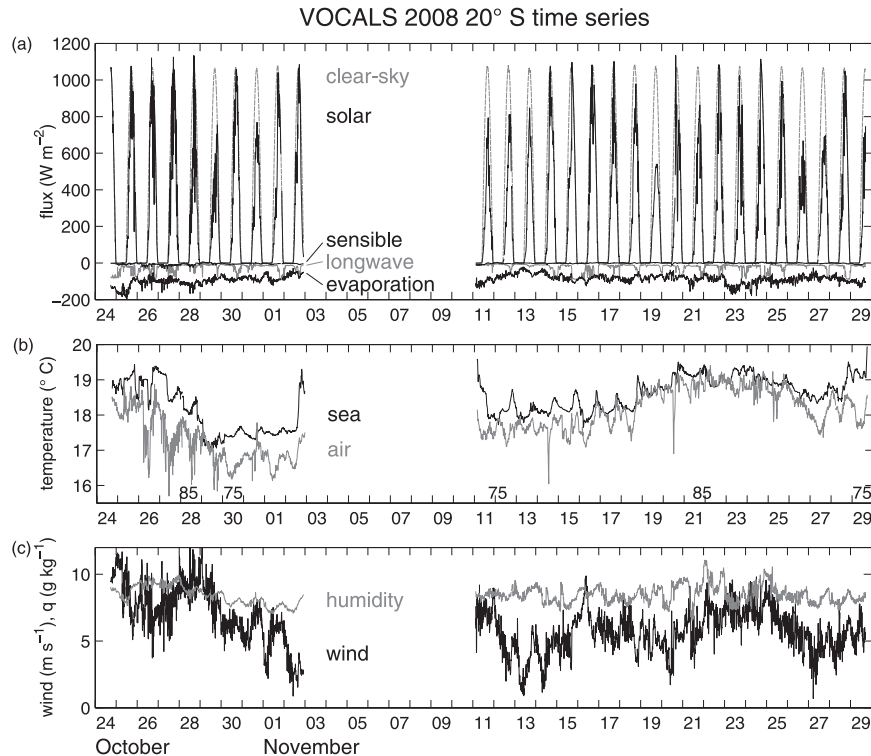
VOCALS 2008 20° S time series

FIG. 2. Time series from VOCALS 2008 found in the stratocumulus synthesis dataset: (a) modeled clear-sky (gray) and observed incident solar radiation, bulk sensible heat flux, net thermal longwave radiatiation (gray), and bulk evaporation; (b) SST from the sea snake and air surface temperature (gray); and (c) specific humidity (gray) and wind speed. Times when the ship was on station at 75° or 85°W are indicated along the bottom axis of (b).

make use of three gridded observation-based air–sea flux datasets available from other researchers, described in section 3. Another aim is to present observations of the surface heat budget along 20°S, 75–85°W from the synthesis dataset (section 4). Section 5 assesses gridded air–sea flux datasets with the ship synthesis dataset. Section 6 assesses the heat budget in 16 coupled climate model simulations in the vicinity of 20°S with the ship data and over the larger southeastern tropical Pacific region with the three gridded flux datasets. Section 7 summarizes the conclusions.

2. The Tropical Eastern Pacific Stratocumulus Synthesis dataset of NOAA ship observations

Research cruises sailed along the 20°S line of latitude in 7 years: 2001 and 2003–07, culminating in the multiplatform Variability of the American Monsoon Systems Ocean Cloud Atmosphere Land Study (VOCALS) Regional Experiment in 2008 (Wood et al. 2007). Scientists and engineers from the National Oceanic and Atmospheric Administration (NOAA) Physical Sciences

Division (PSD) made measurements on these cruises. The capabilities of the NOAA PSD suite of observations are described in Fairall et al. (1997, 2003, 2008). The dates and track of each research cruise used in the synthesis dataset is shown in Figs. 1a and 1b. The observations made on the cruises are the basis of the Tropical Eastern Pacific Stratocumulus Synthesis dataset. This dataset contains continuous 10-min and hourly time series of in situ and remote sensing observations from the ship, and atmospheric upper-air profiles from rawinsondes released several times per day.

Figure 2 presents an example of the 10-min synthesis dataset from the VOCALS 2008 cruises along 20°S. No data were collected 3–10 November while the ship was in port in Arica, Chile. Terms in the surface heat budget (surface solar and longwave radiation, and sensible and evaporative heat flux), modeled clear-sky solar radiation, sea and air surface temperature, air specific humidity, and wind speed resolve the diurnal cycle and the effects of mesoscale weather variability on air–sea interaction. The Tropical Eastern Pacific Stratocumulus Synthesis dataset is further documented in the appendix. In this paper we study the surface heat budget of the

eastern Pacific Ocean using longer-term climatological averages of 10-min flux data.

3. Gridded flux analyses and model data

a. Gridded flux analyses

We use the ship observations at 20°S to verify several gridded flux products available over the global oceans. Each gridded flux product is a unique combination of available model, satellite, and operationally assimilated data. Yu and Weller (2007) of WHOI have used satellite remote sensing and atmospheric reanalyses to produce Objectively Analyzed Air–Sea Fluxes (OAFlux) on a 1° × 1° grid for 1984–2002. The turbulent fluxes are combined with International Satellite Cloud Climatology Project (ISCCP) radiative surface flux data (FD; Zhang et al. 2004), both of which are provided in the WHOI OAFlux dataset.

Large and Yeager (2008) combine historical SST, National Centers for Environmental Prediction–National Center for Atmospheric Research (NCEP–NCAR) atmospheric reanalysis, and ISCCP FD radiative fluxes into a surface flux dataset spanning 1949–2004. The 1° × 1° global dataset is designed for forcing numerical simulations known as Coordinated Ocean–Ice Reference Experiments (COREs). Fluxes in the CORE dataset are adjusted so the net ocean surface flux complies with observed long-term estimates of ocean warming.

University of Washington (UW) researchers provide a turbulent flux dataset for 2000/01 of the tropical Pacific that uses a combination of Quick Scatterometer (QuikSCAT) winds, Tropical Rainfall Measuring Mission Microwave Imager (TMI) SST, and other state variables from reanalysis as inputs into the Coupled Ocean–Atmosphere Response Experiment (COARE), version 3.0, bulk flux algorithm (UW Hybrid; Jiang et al. 2005). State variables used for the flux calculations were chosen from all available variables based on their agreement with observations from the TAO moored buoy array (equatorward of 10° latitude) in the tropical Pacific. Since UW Hybrid data do not contain radiative fluxes, the ISCCP FD radiative fluxes provided by OAFlux are used with UW Hybrid.

b. Coupled models

The International Pacific Research Center (IPRC) Regional Ocean–Atmosphere Model (IROAM; Xie et al. 2007) is a unique coupled regional model that skillfully simulates atmosphere–ocean interactions and clouds in the eastern Pacific (de Szoeke et al. 2006). IROAM is a tropical Pacific Ocean general circulation model forced by reanalysis surface boundary conditions west of

150°W and is coupled to a regional atmospheric model over the eastern Pacific. The atmospheric domain extends over South America and the western Atlantic Ocean to 30°W. Ocean and atmosphere domains extend to ±35° latitude. The atmosphere is relaxed to reanalysis in buffer regions poleward of 30°.

Climate forecasts from coupled GCMs that were used for the Intergovernmental Panel on Climate Change Fourth Assessment Report (AR4) have been archived by the World Climate Research Programme (WCRP) Program for Climate Model Diagnosis and Intercomparison (PCMDI) in the CMIP3 (Meehl et al. 2007). Figure 1b shows the median model SST error in the eastern tropical Pacific for the 15 CMIP3 Twentieth-Century Climate in Coupled Model (20C3M) simulations. In section 6 we assess results in the tropical eastern Pacific from 15 of the CMIP3 20C3M simulations and from IROAM. Table 1 lists the models assessed in this study.

4. Surface heat flux and stress along 20°S, 75°–85°W

The ocean surface heat budget links air–sea fluxes to SST, wind speed, air–sea temperature and humidity differences, and cloud forcing. The stratocumulus cruises along 20°S yield repeatable estimates of the surface heat budget during October–December, a season of strong cloud forcing. Section 4a describes the surface heat budget. Section 4b describes the surface stress.

a. Heat budget

Figure 3 summarizes the surface heat budget along 20°S between the WHOI Stratus buoy at 85°W and the WHOI/Chilean navy tsunami buoy at 75°W. The dots and whiskers show the mean and standard error of the fluxes averaged from the 10-min time series to 2.5° longitude bins (centered at 75°, 77.5°, 80°, 82.5°, and 85°W) for all 7 yr of ship observations.

Sampling variability of the fluxes is larger than the measurement error (less than 10 W m^{-2}), so the accuracy of the mean heat budget is limited by the number of independent measurements. Whiskers show the standard error of the observations in the longitude bins. Standard error is estimated as the standard deviation of all measurements within a longitude bin divided by the square root of 9, the total number of transects across 20°S. This is a conservative estimate for the number of independent measurements and the degrees of freedom for the mean.

Because the ship was underway between 75° and 85°W, diurnal variability can be aliased into the longitude profile. Diurnal cycles of SST, air humidity, temperature, and wind are weak, so diurnal variability is small in all the flux components except for the solar radiation. Solar

TABLE 1. The 16 models compared in this study.

Modeling center	Model name	Model abbreviation	Reference
Canadian Centre for Climate Modelling and Analysis	Coupled GCM, version 3.1	CCCMA CGCM3.1	Flato and Boer (2001)
Centre National de Recherches Météorologiques (France)	Coupled global climate model, version 3	CNRM CM3	Salas-Mélia et al. (2005)
Commonwealth Scientific and Industrial Research Organisation (Australia)	Mark version 3.0	CSIRO Mk3.0	Cai et al. (2005)
Geophysical Fluid Dynamics Laboratory (United States)	Climate model version 2.0	GFDL CM2.0	Delworth et al. (2006)
Geophysical Fluid Dynamics Laboratory	Climate model version 2.1	GFDL CM2.1	Delworth et al. (2006)
Hadley Centre for Climate Prediction and Research (United Kingdom)	Third climate configuration of the Met Office Unified Model	Met Office HadCM3	Gordon et al. (2000a)
Institute of Atmospheric Physics (China)	Flexible Global Ocean–Atmosphere–Land System Model gridpoint version 1.0	FGOALS-g1.0	Yu et al. (2004)
Institute of Numerical Mathematics (Russia)	Climate model 3.0	INM CM3.0	Diansky and Volodin (2002)
L'Institut Pierre-Simon Laplace (France)	Coupled model, version 4	IPSL CM4	Goosse and Fichefet (1999)
Center for Climate System Research (Japan)	Model for Interdisciplinary Research on Climate 3.2, medium-resolution version	MIROC3.2(medres)	Nozawa et al. (2005)
Center for Climate System Research	Model for Interdisciplinary Research on Climate 3.2, high-resolution version	MIROC3.2(hires)	Nozawa et al. (2005)
Max Planck Institute for Meteorology (Germany)	ECHAM5	MPI ECHAM5	Jungclaus et al. (2006)
Meteorological Research Institute (Japan)	Coupled GCM, version 2.3.2a	MRI CGCM2.3.2	Yukimoto et al. (2001)
NCAR (United States)	CCSM3	NCAR CCSM3.0	Collins et al. (2006)
NCAR	Parallel Climate Model, version 1	NCAR PCM1	Meehl et al. (2005)
IPRC (United States/Japan)	IROAM	IROAM	Xie et al. (2007)

radiation was averaged over the whole daily cycle first to remove diurnal aliasing when averaging to longitude bins. The dashed lines show the average of only the five 20°S transects made in late October by cruises in 2001 and 2005–08.

Solar radiation has the largest magnitude in the heat budget, and it is the only term to heat the ocean. Solar heating is more than 200–220 W m^{-2} west of 78°W and 180 W m^{-2} east of 78°W. Since latitude and clear-sky solar radiation is constant across the section, increasing clouds must be responsible for the 30 W m^{-2} difference in the surface solar radiation between 80° and 75°W. All other terms remove heat from the ocean surface. The largest cooling of the ocean surface is the latent heat flux (evaporation), which amounts to −95 W m^{-2} at 85°W and −70 W m^{-2} at 75°W. Over the eight-cruise average, the longitudinal gradient of solar radiation (increasing to the west) is roughly balanced by the gradient of evaporative cooling. The largest solar warming is at 80°W, resulting in a net flux of 120 W m^{-2}. The local maximum at 80°W is not seen in the net flux averaged only from cruises during October (dashed line). The

sensible heat flux is less than 6 W m^{-2} everywhere, and about 2 W m^{-2} between 77.5° and 82.5°W. Longwave radiative cooling of the ocean surface is 25–30 W m^{-2}, without a systematic gradient. The net flux is the sum of the four other flux terms and represents an 85–120 W m^{-2} heating of the ocean surface. This net surface flux would heat a 50-m ocean mixed layer by 1.0°–1.4°C per month.

Our intent is to capture the mean flux over the region, but the ship also samples seasonal, synoptic, and interannual variability. The times indicated by Fig. 1 show that the ship crossed between 75° and 85°W in about two days, in which time seasonal trends would be negligible. The most significant difference between the October average and the average for all cruises is that 10 W m^{-2} less solar radiation is observed during the October cruises. Transects not performed in October were in November and December, and they received more solar radiation, being closer to the southern summer solstice. October cruises also had 10 W m^{-2} more evaporation, resulting in about 20 W m^{-2} less warming in the October cruise average, compared to the all-cruise average. Because the ship travels at about 2.5° per day, it is impossible to
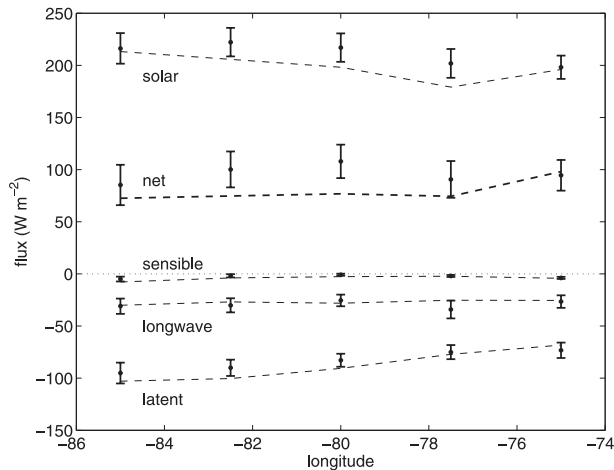
FIG. 3. Longitude-binned (2.5°) surface heat flux averaged from the nine 20°S transects (dots) and the five transects in October (dashed lines). Whiskers are the sampling standard error of the measurements.
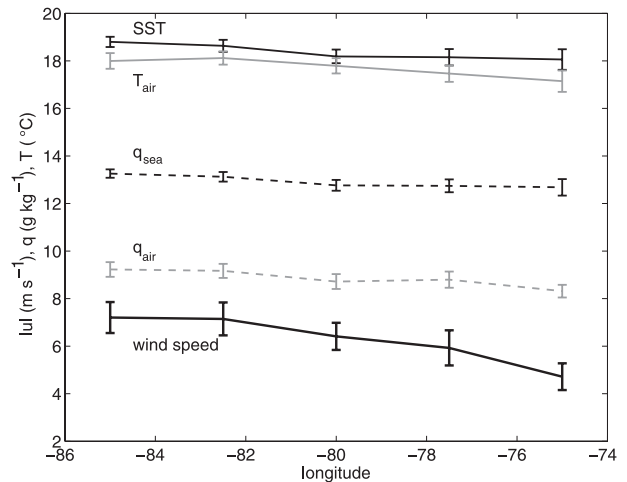

FIG. 4. Longitude-binned factors composing the surface heat fluxes: sea snake SST, air temperature (gray), sea surface saturation specific humidity (dashed), air specific humidity (dashed gray), and wind speed. Whiskers are the standard error of each quantity due to interannual sampling.

diagnose synoptic variability from ship observations alone. After removing the diurnal cycle, solar radiation still has the largest daily-to-interannual variability of ± 20 W m^{-2}. Because daily average clear-sky solar radiation is nearly constant, most of the solar variability is due to clouds. Latent heat flux and longwave cooling both have standard errors on the order of ± 10 W m^{-2}. By averaging together several realizations from different cruises, we expect diurnal, synoptic, and interannual variations to average out relative to the mean.

As context for the fluxes, Fig. 4 shows means of observed quantities for all transects along 20°S. The surface sensible heat flux H and latent heat flux E are proportional to the product of wind speed $|u|$ and sea–air temperature and humidity difference, respectively:

$$H = \rho C_P C_H (SST - T_{air})|u| \quad \text{and} \quad (1)$$

$$E = \rho C_P C_E (q_{sea} - q_{air})|u|, \quad (2)$$

where ρC_P is the density times the specific heat of air at constant pressure, and C_H and C_E are the stability-dependent bulk transfer coefficients for sensible heat and evaporation, respectively. SST, air temperature T_{air}, sea surface saturation humidity $q_{sea} = q_{sat}(SST)$, specific humidity q_{air}, and wind speed all increase to the west along 20°S. Of the quantities relevant to the turbulent heat fluxes, wind speed increases most dramatically, from less than 5 m s^{-1} at 75°W to more than 7 m s^{-1} at 85°W. The change in wind speed explains the gradient of latent heat flux increasing to the west. The relatively small sensible heat flux at 80°W can be explained by the small 0.6°C mean sea–air temperature difference, compared to 1.2°C at 75°W and 0.9°C at 85°W.

The diurnal cycle of the heat fluxes in Fig. 5 has been averaged for ship observations collected along the entire 20°S section between and including the stations at 75° and 85°W. The diurnal cycle is composed by aggregating all observations by their local time into hourly averages. The solar radiation varies from zero at night to 400 W m^{-2} at 1200 LT. The solar radiation R_s is weaker and more reduced in the morning nearer to 75°W (not shown), consistent with more clouds there that clear in the afternoon. The net longwave flux R_l is nearly constant throughout the day, but it is ~15 W m^{-2} stronger in the early afternoon. Evaporation E is 8 W m^{-2} stronger at noon than at its minimum in the hours after sunset. The equation for a diurnal surface layer heat budget is

$$\rho h C_P \partial T/\partial t = R_l + R_s + H + E + \text{residual}. \quad (3)$$

Since h is not measured, we solve for a constant h to characterize the depth of the layer participating in the diurnal cycle of SST. Integrating over the diurnal cycle, the storage $\rho h C_P \partial T/\partial t$ and residual are zero. The solar radiation absorbed in the layer R_s increases with the depth h of the layer, as parameterized by the three-band absorption model of Fairall et al. (1996). A layer with $h = 5.5$ m absorbs 0.62 of the incident solar radiation, balancing the daily net radiative cooling, evaporation, and sensible heat loss.

At night the surface layer cools, with an integrated heat storage of about -80 W m^{-2}. After 0700 LT the surface warms, with peak positive storage of 320 W m^{-2} before 1200 LT. In the afternoon the storage declines, becoming negative after 1500 LT. Advection in the ocean
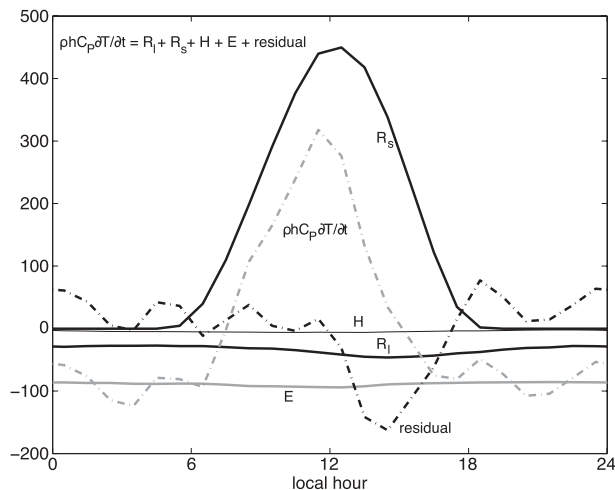
FIG. 5. Diurnal average of the heat budget along 20°S, 75°–85°W. A layer depth of $h = 5.5$ m was assumed for storage ($\rho h C_P \partial T/\partial t$, gray dashed) and the amount of R_s, R_l, H (thin), E (gray), and the residual (dashed) are also shown. Data from all cruises were averaged by local hour.

is represented by the residual in (3). To maintain the modest storage in the afternoon daylight, colder water from beneath 5.5-m depth must be mixing with the surface layer to keep the surface layer cool. This is represented by residual cooling stronger than -100 W m^{-2}. During the rest of the day, the residual is $+0$ to 80 W m^{-2}, indicating mixing from below 5.5 m is helping maintain the layer temperature against constant surface cooling by evaporation and longwave radiation.

b. Surface stress

The southeasterly winds along 20°S are steady in direction and speed. The mean winds and wind stresses in 2.5° longitude bins along 20°S are shown in Figs. 6a and 6b, respectively. The southerly component of the wind was about 4 m s^{-1} everywhere along 20°S, while the easterly component increased steadily from 2 m s^{-1} at 75°W to almost 5 m s^{-1} at 85°W. The ellipses at the end of the wind vectors in Fig. 6a show the standard error of wind components parallel and perpendicular to the mean wind. The standard deviation of the wind was about 1.8 m s^{-1} along the mean wind and 1.5 m s^{-1} across the mean wind, indicating that the wind speed varied slightly more than the wind direction.

Using wind speed and stability measured on the ship, we are able to calculate the wind stress components on the ocean surface. These terms of the momentum budget are important for forcing the large-scale motions of the ocean, and they complement the surface heat budget. Figure 6b shows the wind stress vectors averaged in 2.5° longitude bins along 20°S. The circles and error bars aligned above the tails of the vectors show the
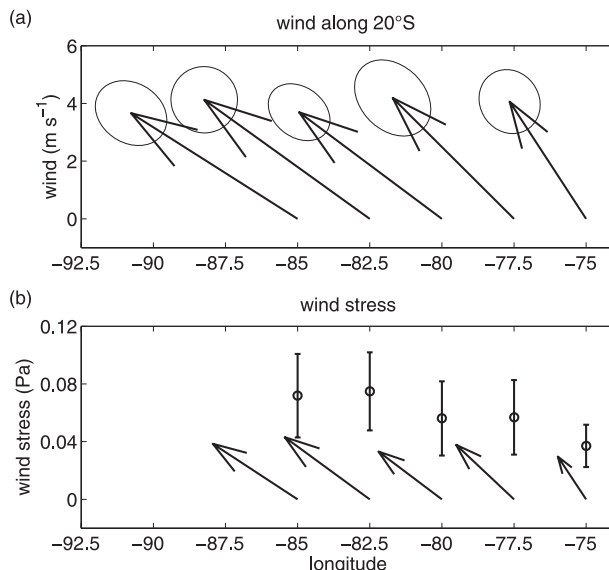

FIG. 6. (a) Wind and standard error of the wind vectors (ellipse) along and across the direction of the mean wind by 2.5° longitude bins. The vertical axis is meridional wind; zonal wind is plotted on the horizontal axis to the same scale. (b) Wind stress vectors, wind stress magnitude (circles), and standard error of the wind stress magnitude (whiskers).

magnitude of the wind stress and its standard deviation. The wind stress magnitude is 0.04 Pa at 75°W and 0.07 Pa at 85°W. The ocean surface current is assumed to be zero in the computation of the wind stress. The expected westward surface current is on the order of 0.2 m s^{-1}, which is negligible compared to the wind speed (4–7 m s^{-1}) in Fig. 4.

5. Evaluation of gridded flux products

Gridded air–sea turbulent fluxes of heat and momentum are computed by three independent research groups at WHOI, UW, and NCAR. In addition to the turbulent fluxes, WHOI includes the ISCCP FD surface flux retrieval, which we also apply to the UW gridded fluxes to compute the total heat flux. The NCAR group adjusts ISCCP FD radiative fluxes to match observed global ocean temperature trends. We now compare and evaluate these gridded flux products.

Figure 7 shows the long-term-average turbulent (left column) and radiative (center column) heat flux in plan view for the three gridded flux products in the eastern tropical Pacific. The right column shows the residual heat flux F_{ocean} that must be supplied by ocean circulation and mixing to make the long-term net storage of the surface layer zero,

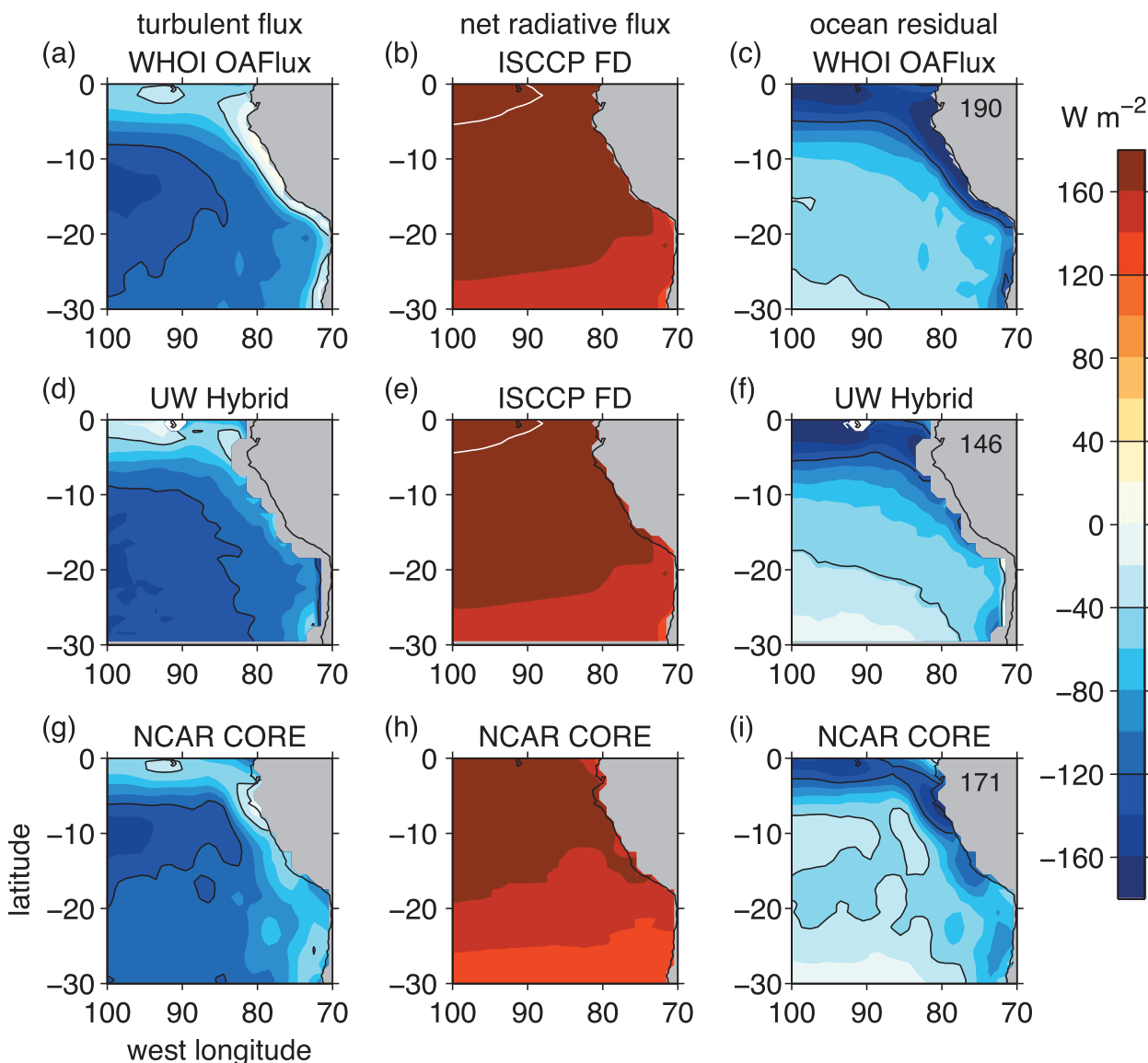$$\rho h C_P \partial T/\partial t = 0 = H + E + R_l + R_s + F_{\text{ocean}}. \quad (4)$$

FIG. 7. (a),(d),(g) Net turbulent, (b),(e),(h) radiative, and (c),(f),(i) residual fluxes from three gridded flux products: (a)–(c) WHOI OAFlux, (d)–(f) UW Hybrid and ISCCP FD, and (g)–(i) NCAR CORE. The three panels for each product (row) sum to zero. The number printed on South America in the residual column is the north–south asymmetry of the residual in the Pacific Ocean east of 90°W and equatorward of 20° latitude.

The sign is such that positive heat fluxes warm the ocean surface, and the sum of all three columns in Fig. 7 is zero.

The three gridded flux products resemble one another. Generally radiative warming (150 W m^{-2}) is balanced by turbulent flux (mostly evaporation), with local reductions in the turbulent flux made up by strong ocean residuals. The most noteworthy features in the surface heat budget are the reductions of turbulent heat flux out of the ocean along the equator and the South American coast. In all three products, turbulent heat flux cooling is weaker than −100 W m^{-2} off the west coast of the Americas. Turbulent cooling is weaker than −40 W m^{-2}

in parts of the equatorial cold tongue and offshore of the Peruvian coast. The radiative flux is relatively uniform across the eastern Pacific, warming the surface by 120–200 W m^{-2}, with radiative warming exceeding 200 W m^{-2} in ISCCP FD in a broad swath along and south of the equatorial cold tongue. The flux datasets require ocean cooling to balance the heat budget. Over most of the eastern Pacific, the ocean residual term is small; however, the ocean cools the surface by more than −120 W m^{-2} in the upwelling regions of the cold tongue and along the coast of Peru. There is a gap with weaker upwelling in the interior of the Arica Bight. Residual cooling of

40–120 W m^{-2} is distributed farther off the South American coast than where mean upwelling is expected.

The NCAR CORE net radiative flux has almost the same shape as the ISCCP FD radiative flux, but it is nearly uniformly 20 W m^{-2} less than ISCCP FD. Within 200 km of the coast of Peru, NCAR CORE has 20 W m^{-2} stronger radiation than farther offshore. ISCCP FD radiative fluxes have a weaker offshore gradient. The increased radiation coincides with a region of low SST and low cloudiness near the coast, which might not be resolved by the ISCCP FD product. In the UW Hybrid product, turbulent flux values have been more conservatively masked, excluding the region of low turbulent flux right along the Peruvian coast. The WHOI OAFlux product has the weakest turbulent cooling. Cooling weaker than −40 W m^{-2} extends along the coast from the equator to 15°S. Some of this reduced cooling in WHOI OAFlux is achieved in NCAR CORE instead by greater radiation warming; however, WHOI OAFlux still has more residual ocean cooling along the coast all the way to 20°S.

The number printed over South America in the ocean residual panels (Figs. 7c, 7f, and 7i) is the area-integrated Northern Hemisphere minus Southern Hemisphere ocean residual flux (terawatts) for the Pacific Ocean east of 90°W and equatorward of 20° latitude. It is positive for all three products because first, the shape of the coastline makes for more ocean area in the Southern Hemisphere in this region. Second, the ocean residual is more negative in the Southern Hemisphere where alongshore trade winds drive coastal upwelling. The flux asymmetry is largest for OAFlux (190 TW) and smallest for UW Hybrid (152 TW), with CORE falling exactly in the middle (171 TW). The smaller asymmetry of UW Hybrid results partly from excluding strong upwelling too close to the South American coast. The 19 TW difference is 11% of the mean flux asymmetry. The differences among the gridded flux products provide an estimate of confidence for comparing flux asymmetry in coupled GCMs.

Figure 8 shows NCAR CORE, WHOI OAFlux, and UW Hybrid gridded flux products, including ISCCP FD radiative fluxes, in comparison with ship and WHOI Stratus buoy observations averaged within 5° latitude of 20°S. Since most of the 20°S transects from the ship were in October, only transects during October (2001 and 2005–08) are included. Ship data have been averaged into 2.5° longitude bins before averaging all October cruises together. These are compared with monthly averages of all available buoy and gridded flux data from October. Figure 9 shows the four terms in the heat budget: turbulent latent heat flux, sensible heat flux, net longwave radiative cooling, and net solar warming, along with the net flux, $F_{net} = E + H + R_l + R_s$, which is the
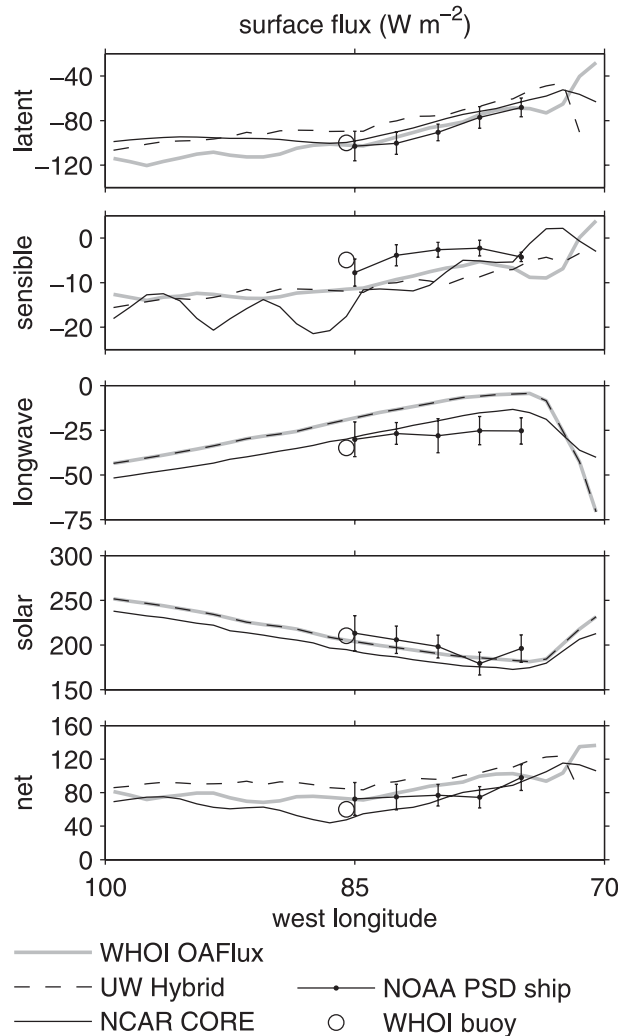

FIG. 8. Mean October surface flux terms over a 5° latitude band centered on 20°S for WHOI OAFlux (1984–2002, gray), UW Hybrid (2000/01, dashed), and NCAR CORE (1949–2004, thin black) gridded flux products, the WHOI buoy (2001–05, circle), and NOAA PSD ship observations with sampling standard error (2001 and 2003–08, whiskers).

sum of the four other terms. Positive values warm the ocean surface. Since there is an annual cycle of mixed layer depth and temperature, there is surface heat storage in the budget in October. Because of the storage, the net surface flux is not balanced only by ocean circulation cooling as it is in the annual average.

The gridded surface flux products agree well among themselves, and with ship and buoy observations. (WHOI Stratus buoy observations have been used to evaluate OAFlux, but ship and buoy observations are not used as inputs into any of the gridded flux products.) Sampling variability within each 2.5° longitude bin was negligible compared to interannual variability of fluxes among
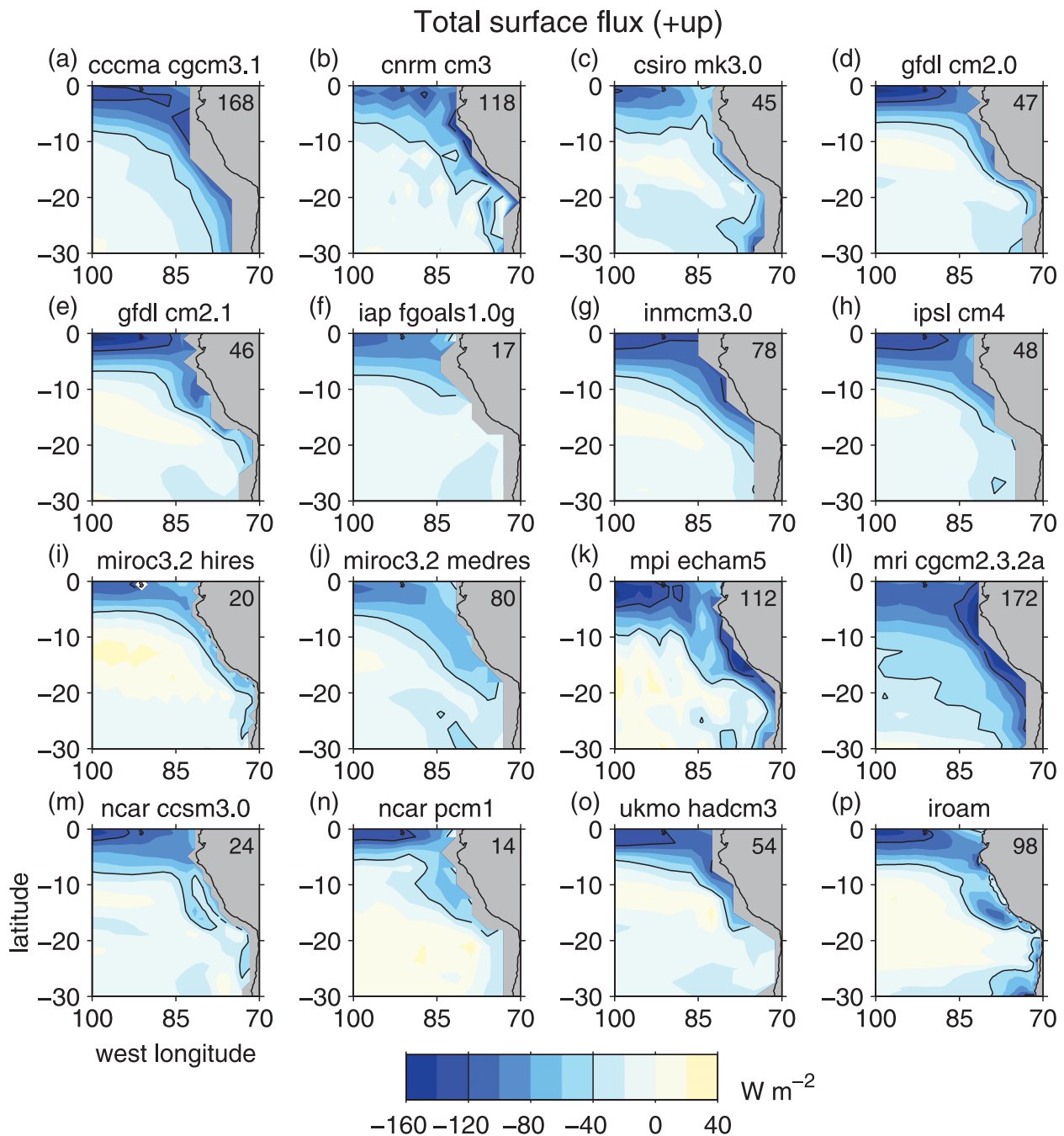
Total surface flux (+up)

FIG. 9. Total surface flux (net R_s, R_l, E, and H) out of the ocean surface climatology over the whole year. Black contour interval is 80 W m^{-2}. Blue (negative) shades indicate the ocean is gaining heat through the surface. Since SST drift is negligible in the long term, this also represents the cooling of the surface provided by the ocean. The number printed on South America is the north–south asymmetry of the residual in the Pacific Ocean east of 90°W and equatorward of 20° latitude.

transects, so the standard errors indicated by the whiskers in Fig. 8 are calculated assuming 1 degree of freedom for each of the five October transects (2001 and 2005–08). Except for sensible heat flux, the flux estimates

from OAFlux, UW Hybrid, and CORE agree with the buoy and ship observations within the interannual sampling error of the cruises. Sensible heat flux is weaker in observations (5 W m^{-2}) than in the gridded products

(10 W m^{-2}), and it has a very small interannual standard error (1 W m^{-2}). Such a small sensible heat flux is near the measurement error of the entire surface heat budget. The ship and buoy measure longwave cooling of about 30 W m^{-2} between 75° and 85°W, with a standard error of about 10 W m^{-2}, which almost encompasses the 15–25 W m^{-2} CORE estimate. The ISCCP FD longwave cooling used by OAFlux and UW Hybrid is 10–15 W m^{-2} weaker than CORE. Solar warming is by far the largest term in the surface heat budget, on the order of 200 W m^{-2}. The 20 W m^{-2} interannual standard error of the solar flux encompasses all the gridded flux products. The ISCCP FD solar flux agrees with the mean solar flux observed on the ship and buoy within half of the interannual standard error. The CORE solar flux is on the order of 10 W m^{-2} lower, implying a more negative shortwave cloud forcing in CORE. It is encouraging that in situ observations and the gridded solar radiation products agree so well, considering documented errors of clouds in coupled models over the southeastern tropical Pacific (Gordon et al. 2000b; Ma et al. 1996; Yu and Mechoso 1999b).

The net surface heat flux into the ocean is about 70 W m^{-2} at 85°W. It is 100 W m^{-2} at 75°W and even larger nearer to the coast. The gradient between 75° and 85°W is consistent among all the flux products and the ship observations. Interannual variations in the net heat flux observed on the ship are on the order of 20 W m^{-2}.

6. Coupled atmosphere–ocean model evaluation

Having established the agreement of three widely available gridded flux products with NOAA PSD in situ measurements from ships in one region, we now compare these products with surface fluxes from coupled models over a larger region. On the basis of their availability and convenience, we have chosen to examine 15 20C3M simulations, archived in a common format by the CMIP3 (Meehl et al. 2007), and the IPRC IROAM.

The residual of surface fluxes shows the cooling required of the ocean to balance the SST tendency at the surface. The residual term contains ocean dynamical cooling and radiation that penetrates the base of the ocean mixed layer before being absorbed. Thus, Fig. 9 can be interpreted as heating and cooling of the surface by ocean upwelling, mixing, lateral transport, and penetrative radiation. For all models in Fig. 9, the ocean residual of the surface heat budget is mostly cooling (negative, blue shades). The expected pattern of ocean cooling in the upwelling is simulated in the upwelling regions along the equator and the coast of South America, yet there are differences among models in the strength and spatial distribution of the cooling. Verifying the

surface heat budget is a valuable diagnostic tool. Upwelling and ocean transport are notoriously difficult to measure directly in the ocean (Colbo and Weller 2007). The surface heat budget residual diagnoses patterns of ocean cooling in observations and models.

Figure 10 shows the surface flux terms, as in Fig. 8, in a column of five axes for each of the 16 models. The fluxes are averaged for the month of October within 5° latitude of 20°S. Each panel also shows the range of observational flux estimates from the three gridded flux products averaged within 5° of 20°S; the WHOI Stratus buoy at 20°S, 85°W; and PSD ship observations between 85° and 75°W.

Common errors are apparent in the simulations. All simulations have too much solar warming, most on the order of 50–100 W m^{-2}. The excess solar warming is compensated by 10–30 W m^{-2} stronger sensible cooling of the ocean surface and about 25 W m^{-2} too much longwave radiative cooling. Excessive solar warming and longwave cooling are consistent with too-weak cloud forcing in simulations. Excessive longwave and sensible cooling are consistent with warm SST errors found in simulations in this region.

The observed profile of solar warming with longitude—or distance from the coast—shows minimum solar warming at 77.5°W, with a gradual increase farther west. Solar warming also increases when approaching the coast from 75°W. This profile corresponds to a maximum of cloud fraction around 77.5°W and to decreased clouds to the west as solid stratocumulus clouds give way to more broken trade cumulus clouds. Coastal clearing is also observed, and it explains the increased solar radiation from 75°W to the coast. Except for the NCAR Community Climate System Model, version 3 (CCSM3), none of the models simulate a solar radiation minimum near 77.5°W. Rather, most models have zonal solar radiation gradients opposite that observed. This reflects the difficulty of coupled models in simulating stratocumulus clouds, especially in shallow boundary layers and poorly resolved coastal transition regions. Observed longwave cooling has the opposite profile of the solar warming: cooling most around 75°W. The observed longwave cooling profile is influenced by the downward emission of thermal infrared radiation by low-level clouds. Failing to simulate clouds well, most models instead have longwave cooling that corresponds most strongly to gradients in SST, with larger net longwave cooling from warmer water farther offshore. While there are large errors in mean evaporative cooling, the zonal gradient of evaporation is relatively consistent among models and observations, with more evaporation from regions of higher SST.

Evaporation, or latent heating, is the strongest cooling term in the budget. The relative error of evaporation
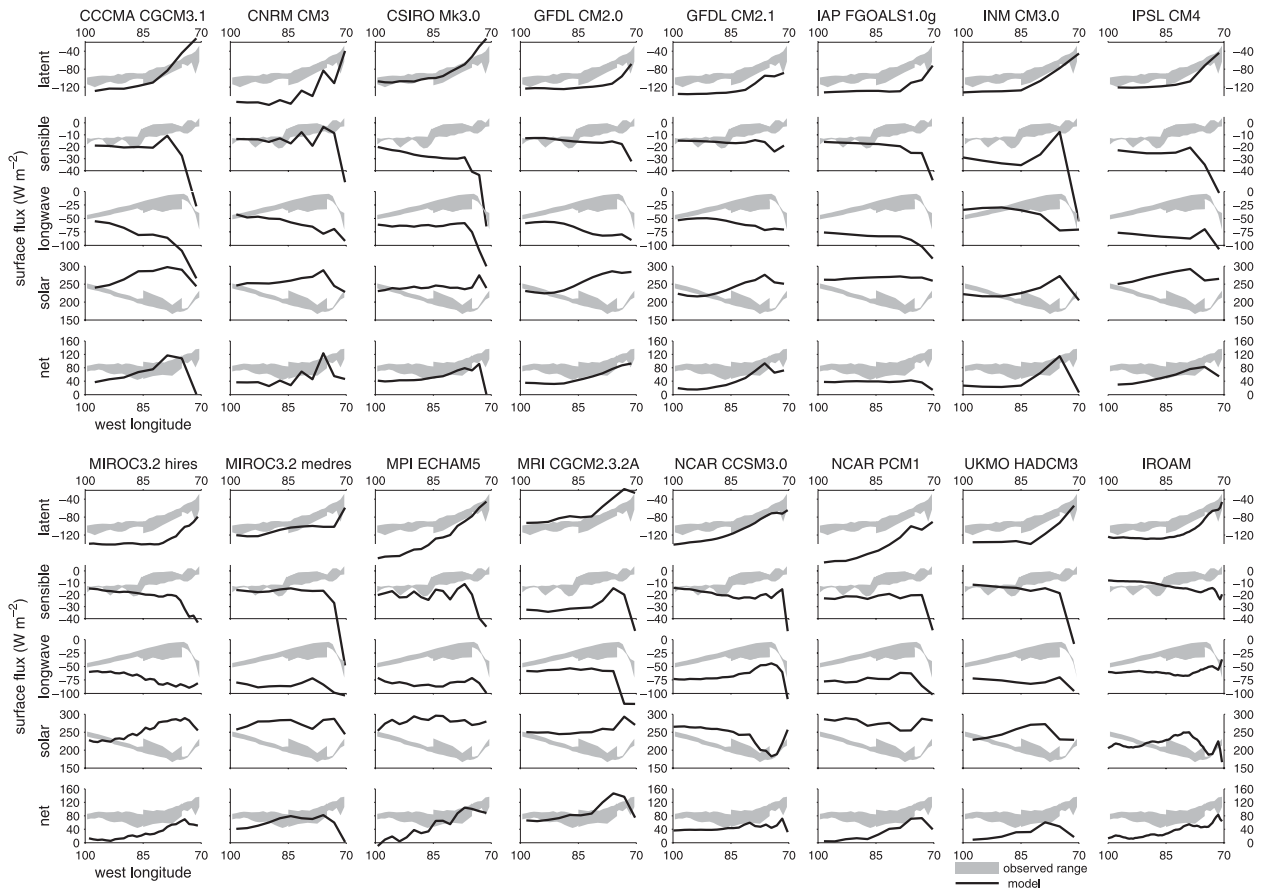
FIG. 10. October 20°S surface flux terms for 16 coupled models compared with the observation-based fluxes. The gray shaded area is the range of the observed fluxes (Fig. 9). Each column of the five panels represents the five flux terms for one model. Modeled flux profiles along 20°S are plotted as thick black lines, and model names are printed at the top of each column.

(typically 30%) is small compared to the relative error of the sensible heat flux (order 100%), but the magnitude of the evaporation is about 5 times that of the sensible heat flux. Evaporation is too strong in 12 of the 16 models. Seven models have evaporation at least 40 W m^{-2} stronger (more negative) than observed. Three simulations have weaker-than-observed evaporation despite stronger sensible cooling. These three simulations must also have a high relative humidity in the southeastern tropical Pacific to inhibit the evaporation relative to the sensible heat flux.

Errors in the net heat flux are small, reflecting the compensation of the excessive solar radiation by stronger longwave radiative cooling and usually stronger latent cooling. Yu and Mechoso (1999a) found that while a coupled GCM adjusted SST away from observations, it did so in a way that maintained evaporation more consistent with observations than an atmospheric GCM over prescribed SST.

The average heat budget for October from 75°–85°W, 15°–25°S is computed for each of the gridded flux products, the ship observations, and the 16 simulations. The heat budget from each dataset is shown in Fig. 11a. Since solar radiation is the largest term in the heat budget, simulated budgets are ranked in ascending order by their solar radiation term. The observationally based gridded flux products and the PSD ship observations have solar flux of 180–200 W m^{-2}, while solar flux simulated by the models is between 240 and 300 W m^{-2}. In the October heat budget (Figs. 10 and 11), the SST tendency is not zero but warms by 0.7°C during the month, according to the 1971–2000 NOAA Optimum Interpolation (OI) SST climatology (Reynolds and Smith 1995). Assuming the mixed layer depth is 50 m (Colbo and Weller 2007), the storage is 50 W m^{-2}. When the storage is written on the same side of the equation as the other terms, it appears as a heat sink, as in Fig. 11. In this way the sum of all heat budget terms in Fig. 11 is zero.

October SST tendency errors are not consistent among models. For convenience we use the observed mixed layer depth of $h = 50$ m to integrate the simulated SST
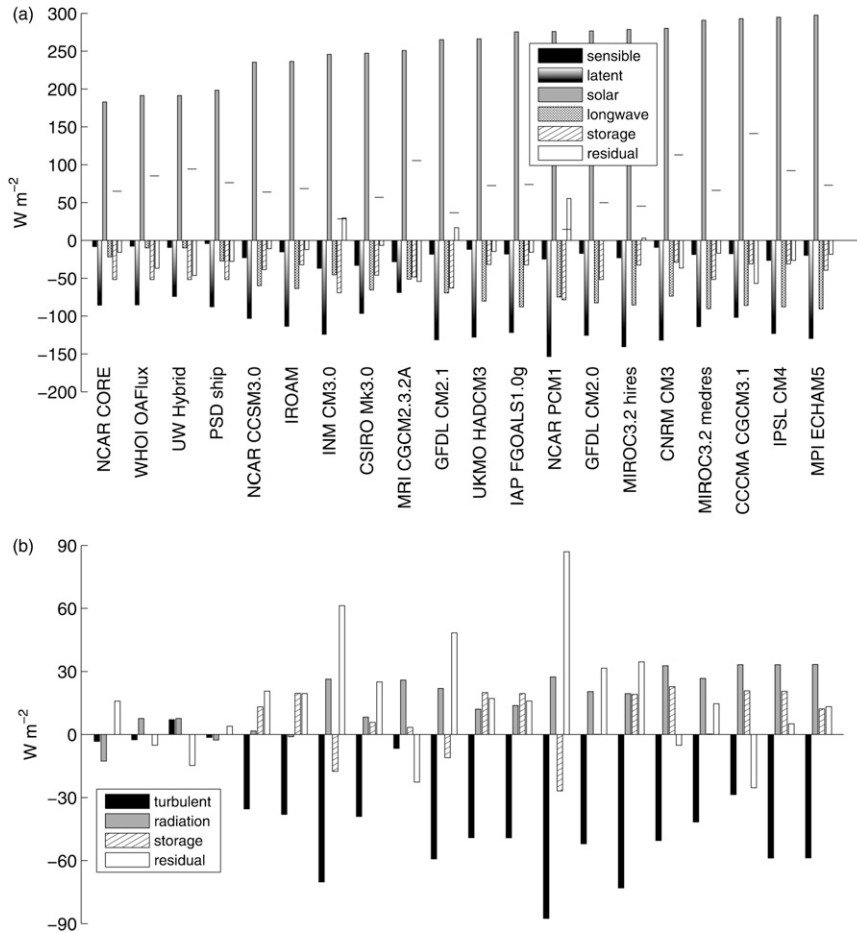
FIG. 11. (a) Total October flux area-averaged between the region 15°–25°S, 75°–85°W for each of the observational products and the 16 coupled models. The observational products and models are ranked according to their solar flux. The storage assumes a mixed layer depth of 50 m. Horizontal lines indicate the mixed layer depth (m) that would be required for the tendency to balance the residual. (b) Heat budget anomalies of (a). The mean of the four observation-based products is subtracted to get anomalies. Sensible and latent heat fluxes are combined into one turbulent flux term, and solar and longwave radiation are combined into one radiative flux term.

tendencies into storage fluxes (W m^{-2}). If the mixed layer depth of the simulation were known, then the mixed layer storage could be derived exactly by scaling the storage in Fig. 11 by the ratio of the simulated mixed layer depth to 50 m. Alternately, the depth required to zero the residual and absorb it entirely into the storage is computed and plotted in Fig. 11a. The observations would require deeper mixed layers, between 50 and 100 m, for the storage to absorb the cooling of the residual. We expect the October residual to be negative, because the residual is negative in the year-round heat budget (Figs. 1 and 8).

Figure 11a summarizes the model errors evident in Fig. 10 at a glance, showing the propensity for models to have too much longwave radiative cooling and solar

heating. Most models also have too much sensible and latent cooling. Here the residual is shown as the heating required so that all six terms balance to zero, opposite the sign of the net flux in Fig. 10. The residual contains ocean dynamical cooling and penetrative radiation. The simulated residual is often found to be weaker than observed, especially for models with weaker solar radiation. Only three models have a residual cooling stronger than observations.

Figure 11b shows the fluxes from the heat budget as anomalies from the mean of the four observational flux products (CORE, OAFlux, UW Hybrid, and PSD ship observations). Because the sensible heat flux is correlated and small relative to the latent heat flux, Fig. 11b combines these into a single turbulent heat flux term.
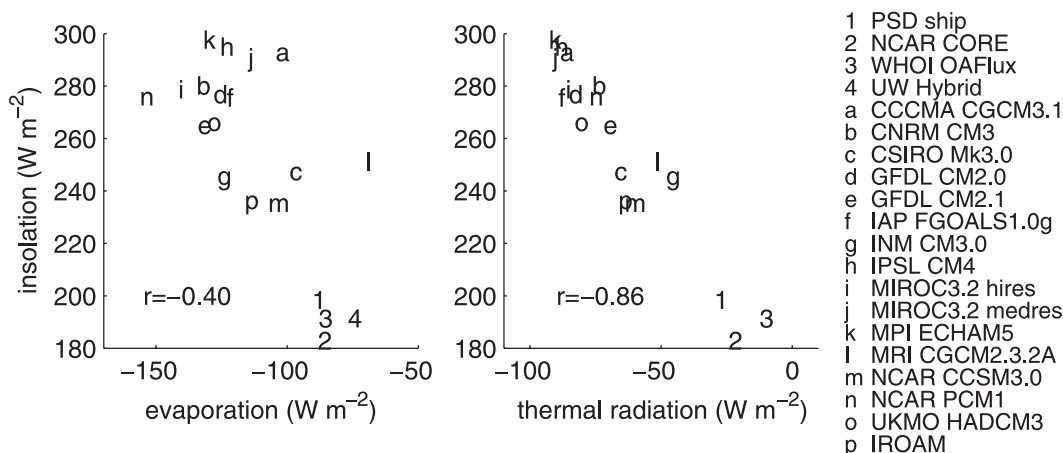
FIG. 12. Scatterplot of fluxes among products and models for the region 75°–85°W, 20° ± 1.25°S: (left) insolation vs evaporation and (right) insolation vs thermal radiation. The four observational products are displayed as numerals, and the 16 models are displayed as letters. Correlations *r* between the fluxes for the 16 models are shown.

Noting the compensation of solar radiation by net long-wave radiative flux, a second simplification combines the radiative flux terms in Fig. 11b. All simulations have turbulent heat flux cooling stronger than the mean of observations. In the two models with the lowest solar radiation, the longwave cooling is strong enough to make the total radiative flux anomaly close to zero. All other models have too much radiative warming. All observations use the storage term from Reynolds SST climatology, so their storage anomaly is zero. There is some variety of the storage term among simulations, so that the ensemble of models has no common systematic error in the storage term. Rather than compensating modestly excessive ($\sim$20 W m^{-2}) radiative warming, the residual term is also anomalously warming in most models, which Fig. 11a showed to be from insufficient residual cooling. These radiative and residual warming anomalies are both balanced by the excessive turbulent heat flux (mostly evaporation), which are systematically the largest errors in the simulations.

The October climatology in Figs. 10 and 11 is compared directly with the ship observations from boreal autumn. Emboldened by the agreement of ship observations with gridded flux products along 20°S in October, in Fig. 9 we compare the ocean residual for coupled model simulations with the three gridded flux products (Figs. 7c, 7f, and 7i) averaged over the annual cycle. Unlike the October climatology, the SST tendency should be negligible when averaged over the whole year, so the residual more accurately represents SST cooling by the ocean. The simulations have the strongest cooling by the ocean on the equator around 100°W and weaker cooling along the South American coast than the flux analyses in Fig. 7. No simulations have cooling stronger

than 120 W m^{-2} connecting the equator to the Peruvian coast. OAFlux and UW Hybrid have 20 W m^{-2} stronger cooling than NCAR CORE, on the order of the difference in the radiation. Cooling in the models is smaller, close to that implied by NCAR CORE. Models in Figs. 9b, 9f, 9i, and 9j have cooling weaker than 120 W m^{-2} everywhere. The north–south asymmetry of the area-integrated ocean residual east of 90°W and equatorward of 20° latitude for each model (terawatts) is printed over South America in the figure. While the asymmetry is 171 ± 19 TW in the gridded flux products, the mean of the models is only 71 TW. Only models in Figs. 9a, 9b, 9k, and 9l have asymmetry stronger than 100 TW. These are the only models to have cooling stronger than 120 W m^{-2} along the Peruvian coast.

The multimodel ensemble of CMIP3 simulations can be treated as a number of separate imperfect realizations of the climate system. Systematic differences in the balance of fluxes achieved by these realizations compared to observations tell us how simulations, each perturbed by imperfections in their physics and external forcing, reach alternate climate equilibria.

Figure 12 shows surface insolation heating versus evaporation and net longwave thermal radiation—the strongest two cooling surface flux terms—along 75°–85°W, 20° ± 1.25°S. ISCCP FD provides insolation to the UW Hybrid and WHOI OAFlux datasets. Letters indicate terms for each of the models, and each of the observational datasets is indicated by a number. There is a tendency for models to have stronger-than-observed insolation and evaporation, with models clearly separated from the observations in Fig. 12a. Models with higher insolation along 20°S tend to have stronger surface cooling from evaporation and thermal radiation; however,

excluding observations, the correlation between evaporation and insolation among models ($r = 0.40$) is not statistically significant. Correlations among the 16 models are significant at 95% confidence when their absolute value exceeds 0.50. The correlation of surface insolation to net thermal radiation among simulations is -0.86. Insolation anomalies are linked to longwave radiation in two ways. First, positive solar radiation anomalies affect the surface by warming SST, which results in stronger thermal radiative cooling of the surface, as indicated by the significant correlation of SST to net longwave radiation ($r = -0.58$, Fig. 13b). Second, low clouds reduce solar radiation by obscuring sunlight from reaching the surface and simultaneously reduce the net thermal radiative cooling by emitting thermal radiation back to the surface. In fact, the correlation among models of downwelling solar to downwelling longwave radiation is -0.74. According to their covariance among models, two thirds of the insolation anomalies are compensated by net thermal radiation anomalies.

Figure 13a shows the insolation versus SST in observations and CMIP3 simulations along 75°–85°W, 20° ± 1.25°S. We would expect that models with fewer clouds that admit more solar radiation to the surface also have warmer SST along 20°S. The correlation among models of SST to solar radiation is 0.31. The correlation is weak, perhaps because of the divergent representation of clouds in these simulations. The models exhibit average SST along 20°S in a range from 17.5° to 21°C, while observations show SST just below 18°C. Insolation sampled by the ship (200 W m^{-2}) was larger than the October average of CORE or ISCCP but 30 W m^{-2} less than the nearest simulation.

Figure 13c shows significant correlation of latent heat flux to SST (-0.60) among the models. The negative correlation indicates that evaporation responds to SST as a negative feedback, cooling warm SST anomalies.

The correlations mentioned earlier do not include the four observational datasets also shown in Fig. 13. Insolation and thermal radiation observations are visibly distinct from the models. Insolation in the models is 40–100 W m^{-2} higher than observations. Models g, c, and l have SST less than 18°C, close to observations. Each model g, c, l, m, and p has weaker insolation and weaker net thermal radiative cooling than the other models, which is probably the result of more low clouds in their simulations.

All the models except for model l have stronger evaporation than observed. The model n has the strongest evaporation—70 W m^{-2} stronger than observed—and has among the highest SST (20°C). Thermal radiation in the models is -40 to -90 W m^{-2} (cooling); however, in the observations it is weaker than -30 W m^{-2}. The flux anomalies of the models relative to observations
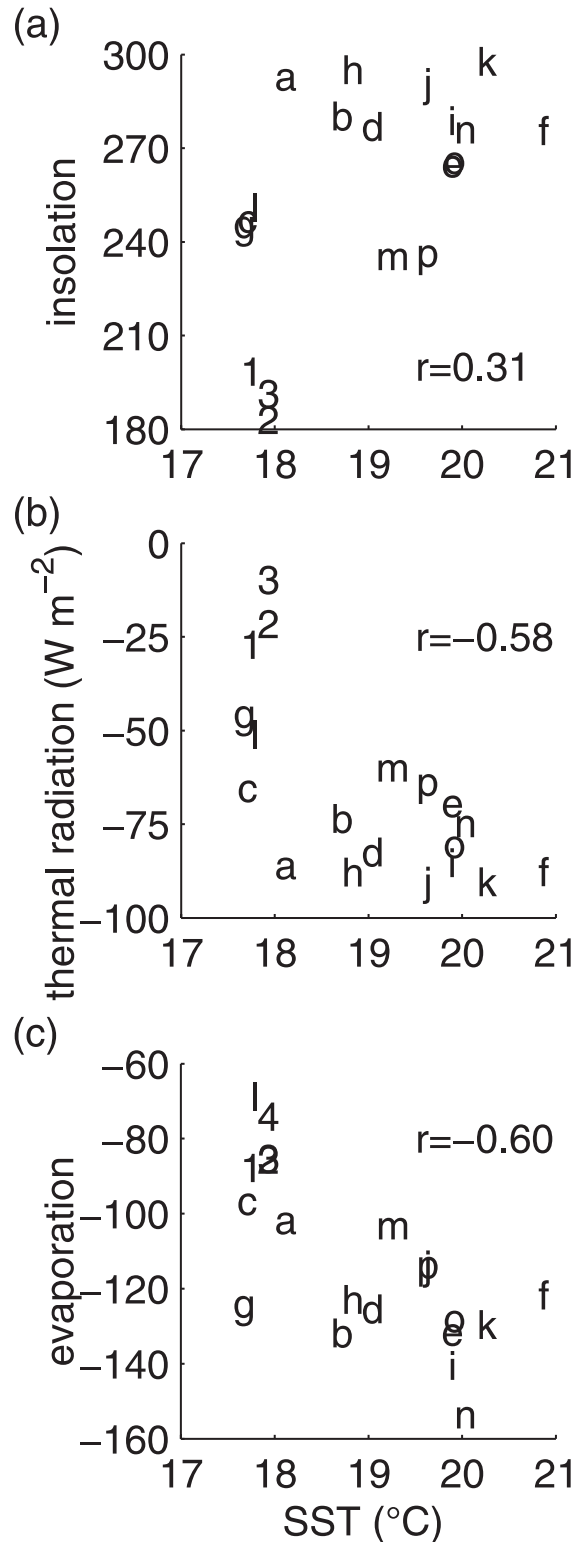

FIG. 13. Scatterplot of (a) insolation, (b) thermal radiation, and (c) evaporation, vs SST for observations and the 16 models in the region 75°–85°W, 20° ± 1.25°S. Model symbols are as in Fig. 12. Correlations r between the fluxes for the 16 models are shown.

are consistent with positive SST errors and insufficient clouds in the models.

7. Summary

Research ships made nine transects along the 20°S parallel in the tropical eastern Pacific Ocean in 7 years between 2001 and 2008. Observations of surface fluxes, surface meteorology, and clouds were made, as well as rawinsonde profiles of the atmosphere. These observations have been arranged to common coordinates and stored in efficient network Common Data Form (netCDF) binary and American Standard Code for Information Interchange (ASCII) text formats to facilitate their comparison with other observations, gridded analyses, derived products, and coupled models.

Air–sea fluxes computed from in situ bulk surface oceanic and meteorological observations are used to independently verify new gridded datasets of heat fluxes over the ocean in this climatically important region. Three gridded heat flux products tested—NCAR CORE, WHOI OAFlux, and UW Hybrid—agree well with the average of ship observations over 7 years, giving us confidence that the limited sampling by the ship is nonetheless a representative climatology, and that the gridded flux datasets perform well in this region where climate models are known to exhibit errors.

Observational flux datasets agree among themselves, with small differences from the mean observed fluxes (Fig. 11b). UW Hybrid latent heat flux is about 10 W m^{-2} weaker than the others. The NCAR CORE radiative flux is about 20 W m^{-2} weaker than the others. Anomalies of the residual term tell how well the four estimates of the flux agree on the net heat balance. The standard error of the residual is 6 W m^{-2}, indicating excellent agreement of the net budget in the four datasets, with anomalies on the order of expected measurement error.

The observational flux datasets imply subsurface cooling must balance the ocean surface heat budget along 20°S, 75°–85°W. Cooling in the southeastern Pacific Ocean has been proposed to result from mixing by shear associated with near-inertial oscillations (e.g., Halpern 1974), or from eddy heat flux divergence (Colbo and Weller 2007). Eddy-permitting and eddy-resolving models of the southeastern Pacific Ocean show horizontal eddy heat flux divergence to be small in the regional average, with geostrophic transport due to salinity gradients contributing most of the cooling (Toniazzo et al. 2010; Zheng et al. 2010).

All eight cruises were in boreal autumn. Five of the cruise transects were in October, the two in 2003 and 2008 were in November, and the one in 2004 was in December. Differences in the climatology of the 20°S transects were small between averaging all transects from October to December and averaging only those in October. Slight changes in the season of the cruise result in sampling differences on the order of variations among years when the ship sampled in October. Though 7 yearly samples are enough to have a reasonable seasonal mean, this time span samples only about two realizations of El Niño–Southern Oscillation (ENSO)—not enough to sample distinct phases of interannual variability.

Sampling differences among cruises were on the order of differences among the observation-based datasets, and they were considerably smaller than differences seen among coupled climate models or between these models and observations. Therefore, the ship data samples the mean boreal autumn well enough for the purpose of verifying and assessing the current generation of general circulation models. On the basis of their agreement with the ship data in boreal fall, we expect the three gridded flux datasets are also sufficiently accurate for verifying climate model simulations. Confidence in the gridded flux datasets in this challenging region is particularly useful, as the gridded data facilitate broader evaluation of models.

For decades the eastern tropical Pacific region has been a challenging test for coupled climate models. Ship and satellite observations of October SST along 20°S between 75° and 85°W are about 18°C, while CMIP3 coupled models simulate SST in the range of 17.5°–21°C. All but 3 of 16 models have a warm SST error on this transect. Hundred-year climate simulations whose SST differ from observations reach a heat balance that requires this alternate equilibrium SST.

All coupled climate simulations assessed have excessive insolation and thermal radiative cooling on the order of 20 W m^{-2}, suggesting that all the simulations have too few or radiatively ineffective clouds. Because solar warming and thermal radiative cooling are of opposite sign, there is compensation between the errors and little correlation with SST. Even models g, c, and l, with SST close to observations, have compensating errors between excess solar warming and thermal radiative cooling (Figs. 13a,b). According to the covariance in the model ensemble, two-thirds of the insolation anomaly tends to be compensated by increased thermal radiative cooling of the ocean surface (Fig. 10).

When the compensation of solar and longwave radiative errors is taken into account, the ensemble mean net excess radiation is about 20 W m^{-2}. Most model simulations have too much latent and sensible heat flux. Excess evaporation of about 40 W m^{-2} is usually the largest error term in the model heat budget. This heat balance implies simulated oceanic cooling weaker than observations, suggesting many models inadequately represent surface cooling from oceanic upwelling, entrainment, and eddy transport.

APPENDIX

Documentation of the Synthesis Dataset

Time series of measurements and derived variables at 10-min and hourly resolution are available from the Tropical Eastern Pacific Stratocumulus Synthesis dataset. Measurements comprising the dataset were made on ship cruises in the southeastern tropical Pacific Ocean to the WHOI Stratus buoy at 20°S, 85°W (hereafter stratocumulus cruises). This appendix documents the instrument(s), sampling frequency, analysis techniques, units, estimates of accuracy and resolution, and particular configurations on different cruises used for each of the variables in the stratocumulus synthesis dataset.

Appendix section *a* describes in situ flux and meteorological observations. Appendix section *b* describes cloud remote sensing from NOAA PSD portable cloud-observing systems. Appendix section *c* explains how these observations from all the cruises have been arranged and synchronized into a unified time series, and it describes the calculation of derived variables in the synthesis. This time series comprises the first half of the synthesis dataset. Appendix sections *d* and *e* document each of the variables stored in the dataset. Appendix section *f* documents the second half of the synthesis dataset, composed of data retrieved from rawinsondes released from the ship.

a. Flux and surface meteorology observations

Instruments mounted to the forward mast at the bow of the ship measure near-surface wind, temperature, and humidity. Wind velocity is measured with a sonic anemometer at 17.5 m above sea level. The speed and course of the ship are added to the anemometer wind to get the earth-relative wind. Temperature and humidity are measured with a Vaisala HMP-235 or HMT-335 thermometer/ hygrometer, aspirated and shielded from radiation, at 14.8 m above mean sea level. The Vaisala sensors have an accuracy of 0.1°C for temperature and ≤2% for relative humidity. SST is measured by a "sea snake" thermometer floating ~5 cm below the water surface. The sea snake temperature measurement resolves solar warming of the near-surface layer of the ocean but not the evaporative cool skin effect on the surface. Rain at the ship is measured by an optical scintillation rain gauge. Surface fluxes of downwelling solar and thermal infrared radiation are measured by Eppley Precision Spectral Pyranometers (PSP) and Precision Infrared Radiometers (PIR), respectively. The radiometers are situated ~2 m above one of the upper decks of the ship, so as to minimize their view of the ship superstructure. Case and dome temperatures are measured by the PIR to convert thermocouple voltage into downward radiation, with a precision of 1.5% (Fairall et al. 1998). A Campbell Scientific datalogger samples these slow meteorological sensors every second and averages them for 1 min. One-minute averages are saved to disk by a data acquisition personal computer (PC) synchronized to a global positioning system (GPS) clock.

A second set of instruments on the forward mast measures atmospheric wind and scalars at 10 Hz, enabling direct computation of fluxes by the covariance method. The sonic anemometer and motion package are capable of measuring the three components of velocity and temperature at 10 Hz. A GPS receiver and an inertial motion sensor located near the anemometer register the vector motion of the ship, which is added to the sonic anemometer wind to get earth-relative wind (Edson et al. 1998). Fast optical LI-7500 open-path gas analyzers by LI-COR retrieve water vapor and carbon dioxide concentration from differential absorption of three infrared wavelengths. Turbulent fluxes are also estimated using the COARE 3.0 bulk flux algorithm (Fairall et al. 2003). At the time of writing, the synthesis data contain bulk fluxes only.

b. Cloud and aerosol observations

In addition to the solar and infrared radiometers, NOAA PSD uses remote sensing at several wavelengths to detect cloud and integrated liquid water properties in the atmosphere.

The cloud top is the coldest place in the marine atmospheric boundary layer (MABL), due to the adiabatic (or moist adiabatic) profile of the MABL and strong thermal infrared radiative cooling at the cloud top. Clouds that penetrate into the inversion quickly evaporate due to warm dry air in the inversion. Because the inversion is distributed over a finite depth of 100–200 m, the center of the inversion is slightly higher than the top of the stratocumulus cloud capping the MABL. The inversion base, defined as the temperature minimum separating the MABL from the capping inversion, is coincident with the top of the cloud and the local temperature minimum. Both the center of the inversion (maximum gradient) and the inversion base (minimum temperature) can be found from the temperature profile from rawinsondes released every 4–6 h.

Boundary layer inversion height is retrieved more frequently by the NOAA 915-MHz Doppler radar wind profiler aboard the NOAA ship *Brown*. The profiler operated on every research cruise except in 2003. Radar pulses are scattered by refractive index gradients in turbulent eddies, generated by strong mean gradients at the inversion. Reflectivity and Doppler moments are computed at approximately 1-min resolution in 60-m range gates. The maximum radar reflectivity at range gates between 600 and 1500 m was taken to indicate the sharp temperature and humidity gradient at the height of the inversion (Angevine et al. 1994; Bianco and Wilczak 2002). The inversion height for a 10-min interval is the median height of maximum radar reflectivity.

Cloud-top height coincides with a temperature minimum 50–100 m below the center of the inversion layer. A vertically pointing 8.6-mm wavelength cloud radar (MMCR) with a 37-m range gate was used to estimate cloud-top height for 2001, 2003, and 2004, while a W-band radar (3.17-mm wavelength) with a 25-m range gate was used in 2008. Comparisons with radiosonde temperature and humidity profiles show the cloud-top height agrees with the inversion base height to the ~25-m resolution of the measurements.

Cloud base and cloud fraction are measured by a Vaisala lidar ceilometer. The ceilometer retrieves cloud base heights every 15 s for up to three cloud layers with 15- or 30-m resolution. The lowest cloud base usually represents the base of the stratocumulus layer; however, it occasionally represents the base of intermittent cumulus rising into stratocumulus. The 15th, 50th, and 85th percentiles of the lowest cloud base are recorded in the synthesis dataset for every 10-min interval. Cloud fraction is computed from the ceilometer as the fraction of 15-s samples in the 10-min interval for which a cloud is detected.

Passive microwave radiometers retrieve column-integrated water vapor and liquid water from brightness temperature measurements at multiple wavelengths. A two-channel (23.8 and 31.4 GHz) Radiometrics "mailbox" radiometer, a prototype to those used by the Atmospheric Radiation Measurement Program (ARM; Stokes and Schwartz 1994), was used aboard the ship in 2001 and 2005–07, and a newer mailbox lent by Dr. Peter Minnett was used during the 2008 cruise. In 2001, 2003, and 2004, a Hughes (20.6 and 31.65 GHz) radiometer was used. The radiometers perform tipping calibrations, which provide reference brightness temperatures when no liquid water is present. Brightness temperatures are postcalibrated using tipping calibrations only from clear-sky conditions (Han and Westwater 2000; Westwater et al. 2001). Valid tipping calibrations can be infrequent in this region, because stratocumulus clouds typically cover the sky. Column-integrated water vapor is empirically proportional to a weighted sum of the ~20- and ~30-GHz optical thicknesses. Primarily to account for cloud temperature in the integrated liquid water retrieval, a forward radiative transfer model is run using a nearly contemporaneous radiosonde profile of temperature and humidity. Cloud water in the model is varied iteratively within the cloud boundaries until the modeled microwave brightness temperatures match those of the radiometer (Zuidema et al. 2005). Given infrequent calibrations and drifts in instrument sensitivity, except for 2008, the liquid water path accuracy is more uncertain than is typical for ARM radiometers.

A Particle Measuring Systems LASAIR II-110 draws air through an optical forward scattering probe and counts aerosol particle concentration in six diameter bins: 0.1–0.2, 0.2–0.3, 0.3–0.5, 0.5–1.0, 1.0–5.0, and >5.0 μm. The LASAIR particle counter was used in 2003 and 2005–07. Smaller (Aitken mode) aerosols were measured by investigators from Texas A&M University (TAMU) in 2003 and 2004, and by Pacific Marine Environmental Laboratory (PMEL) in 2008. Particle number measurements agree between TAMU and the PSD LASAIR particle counting systems in 2003. For the synthesis, three size bins were chosen to be uniform across both platforms: 0.1–0.3, 0.3–1.0, and >1.0 μm. No aerosol measurements were made in 2001.

c. Time series and derived variable processing

Synthesis data from the diverse instruments are presented as averages within uniform 10-min time intervals. Clocks on the various instruments were synchronized daily to the GPS clock. Clock drift over a day is less than a few seconds, negligible compared to the 10-min interval. Times of maintenance (e.g., cleaning the solar and infrared radiometer domes and rinsing the LI-7500 water vapor/CO_2 sensor window) and known sensor

malfunction are masked out, as well as out-of-range values in the data stream. The remaining valid data within the sampling interval for each instrument are used to compute the 10-min mean, in such a manner that time integrals of the data are conserved. Data are likewise averaged to hourly intervals. The 10-min and hourly time series data are provided in netCDF and ASCII text formats.

Bulk turbulent fluxes in the stratocumulus synthesis dataset use air temperature and humidity from the Vaisala sensor, SST from the sea snake thermometer, and wind data from the motion-corrected sonic anemometer. Turbulent fluxes appearing here and in the synthesis dataset are 10-min or longer averages of fluxes computed with the COARE 3.0 bulk flux algorithm (Fairall et al. 2003) from 5- or 10-min averages of near-surface wind, humidity, and temperature measurements. Radiative fluxes are averaged over the same 10-min intervals. The COARE 3.0 flux algorithm models the evaporative cool skin effect on ocean surface skin temperature. Upwelling radiation can be modeled by a sea surface albedo of 0.05 for solar radiation and Stefan–Boltzmann emission for longwave radiation, with a surface emissivity of 0.97. Cloud transmissivity, optical depth, and radiative forcing are found by comparing observed radiative fluxes with radiative fluxes that would be observed under clear skies. As in Fairall et al. (2008), downwelling clear-sky radiation is computed by the radiative transfer model of Iqbal (1988).

The Tropical Eastern Pacific Stratocumulus Synthesis dataset is available for download from the NOAA Earth System Research Laboratory (ESRL) PSD Web site (available at http://www.esrl.noaa.gov/psd/psd3/synthesis/). The following lists describe the time series variables available in the stratocumulus synthesis data.

d. Independent variables

1) *Gregorian year* (yr). Year for the time stamp.
2) *Yearday.* Days (UTC) since 31 December of prior year of the start of the time stamp. This time corresponds to the beginning of an hourly or 10-min interval.

e. Dependent variables

3) *Latitude.* Decimal degrees, positive north latitude, from NOAA ESRL PSD GPS. Accurate to 100 m.
4) *Longitude.* Decimal degrees, positive east longitude, from PSD GPS. Accurate to 100 m.
5) *Thermosalinograph sea chest water temperature* (°C). Temperature measured by a Sea-Bird thermosalinograph in the ship's sea chest. Seawater is

pumped through the sea chest from an intake in the hull approximately 5 m below the sea surface. Accurate to ±0.001°C.
6) *Sea snake water temperature* (°C). SST from the PSD sea snake floating thermistor. The thermistor floats at 0.05-m depth when the ship is stationary. At this depth, the sea snake samples the solar warm layer but not the cool skin effect. Accurate to ±0.1°C.
7) *Air temperature* (°C). Air temperature measured by a Vaisala HMP-300 series probe maintained by PSD on the forward mast, 14.8 m above sea level. The temperature sensor is housed in a radiation shield and aspirated by an electric fan. Accurate to ±0.1°C.
8) *Westerly wind component* (m s^{-1}). Earth-relative mean zonal wind. Relative heading and motion of the ship is computed from the GPS and added to the ship-relative wind measured by a Gill sonic anemometer at 17.5 m above mean sea level on the forward mast. Accurate to ±2%.
9) *Southerly wind component* (m s^{-1}). Earth-relative mean meridional wind. Relative heading and motion of the ship is subtracted from the ship-relative wind from the sonic anemometer. Accurate to ±2%.
10) *Scalar wind speed* (m s^{-1}). Earth-relative average scalar wind speed from the Gill sonic anemometer. Vector winds averaged to 1 min are converted to scalar wind speed, which is averaged for 10 min. Accurate to ±2%.
11) *Sensible heat flux* (W m^{-2}). Positive-upward sensible heat flux computed from the COARE 3.0 bulk flux algorithm. Scalar wind speed, skin sea surface temperature, and air temperature are the most important inputs for computing the bulk fluxes.
12) *Latent heat flux* (W m^{-2}). Positive-upward latent heat flux (evaporative heat flux) computed from the COARE 3.0 bulk flux algorithm.
13) *Bulk wind stress* (Pa). Wind stress magnitude on the ocean computed from the COARE 3.0 bulk flux algorithm. Ocean currents are assumed to be zero, and bulk stress is assumed to be in the direction of the mean wind.
14) *Rain rate* (mm h^{-1}). Rain rate from an Optical Scientific, Inc. optical scintillation rain gauge mounted at 14.8 m above mean sea level on the forward mast.
15) *Thermal infrared (longwave) radiative flux* (W m^{-2}). Positive-downward longwave (thermal infrared) radiative flux measured as the average of two Eppley Precision Pyrgeometers. Radiometers are mounted on a sea container on the 02 deck high enough to minimize their view of the ship superstructure. Accurate to ±2 W m^{-2}. Dome and housing temperatures from thermistors inside the solar and thermal infrared radiometers are adjusted to agree with the

more-precisely calibrated Vaisala air temperature sensor at night, when the radiometers are in equilibrium with the air temperature.

16) *Clear-sky thermal infrared (longwave) radiative flux* (W m^{-2}). Positive-downward clear-sky longwave radiation computed from the model of Iqbal (1988). Water vapor path estimated from the microwave radiometers is used by the radiative transfer model.

17) *Downward solar radiative flux* (W m^{-2}). Positive-downward solar radiative flux measured as the average of two Eppley Precision Pyranometers. Accurate to ±2 W m^{-2}.

18) *Clear-sky solar radiative flux* (W m^{-2}). Positive-downward clear-sky solar radiative flux computed from the model of Iqbal (1988). Water vapor path estimated from the microwave radiometers is used by the radiative transfer model.

19) *Fifteenth percentile of cloud base height* (m). Cloud-base height from a Vaisala lidar ceilometer, sampled every 15 or 30 s. Fifteen percent of cloud bases sampled in the 10-min interval are below the 15th percentile cloud height.

20) *Median cloud base height* (m). Cloud-base height median from a Vaisala lidar ceilometer.

21) *Eighty-fifth percentile of cloud-base height* (m). Cloud-base height from a Vaisala lidar ceilometer, sampled every 15 or 30 s. Fifteen percent of cloud bases in the 10-min interval are *above* the 85th percentile cloud height.

22) *Inversion height* (m). The NOAA wind profiler receives strong backscatter from temperature and humidity gradients in the MABL inversion. The inversion height is the height of the strongest backscatter in the upper MABL and lower free troposphere. The inversion height from the NOAA wind profiler agrees with the center of the inversion from rawinsonde profiles. When the NOAA wind profiler is not available, the inversion height is interpolated from the 4–6 hourly rawinsonde profiles.

23) *Inversion base height* (m). The inversion base height is determined from soundings every 4–6 h as the height of the temperature minimum at the base of the inversion layer. The inversion base height is found to coincide with the top of the clouds from cloud radar retrievals within the precision of the instruments. This is filled with missing values except when a sounding crosses the inversion base height within the time interval.

24) *Cloud-top height* (m). When there is a cloud, cloud-top height is determined from cloud radar (MMCR or W-band) as the height above which the radar reflectivity falls below a threshold based on the minimum detectable signal of the cloud radar.

Cloud radars were operated in 2001, 2003, 2004, and 2008. Accuracy is limited by the range resolution of the instrument, which is 37 m for the MMCR and 25 m for the W-band radar. In 2001, 2004, and 2008, cloud radar and the NOAA profiler operated simultaneously, and cloud-top heights from the MMCR were found to be 50–100 m below the inversion height from the profiler.

25) *Cloud thickness* (m). Difference between best estimate of cloud top height and stratocumulus cloud base height. Cloud base heights are statistically filtered to remove most of the bases of boundary layer cumulus below the stratocumulus layer.

26) *Cloud optical thickness* (unitless). Cloud optical thickness for solar wavelengths is computed by matching the Stephens et al. (1984) cloudy-sky model to the observed transmission coefficient. Visible irradiance is decreased through the cloud by a factor of the natural exponent of the optical thickness.

27) *Liquid water path* (g m^{-2}). From the microwave radiometer. Cloud liquid water path is determined from two passive microwave wavelengths (approximately 10 and 15 mm) by iteration of a radiative transfer model in the physical retrieval method of Zuidema et al. (2005).

28) *Cloud fraction* (unitless). Fraction of time in the interval when the lidar ceilometer detected a cloud directly overhead.

29) *Cloud drop number* (number cm^{-3}). Number of cloud drops deduced from the cloud optical thickness, liquid water path, and solar zenith angle by the optical microphysical model of Dong et al. (1998).

30) *Aerosol number with diameter* $0.1 < D < 0.3 \times 10^{-6}$ m (number cm^{-3}). Aerosol measured at the surface with diameter greater than 0.1×10^{-6} m and less than 0.3×10^{-6} m. In years 2005–07, a Particle Measuring Systems LASAIR II-110 particle counter was used. The LASAIR II-110 particle counter measures scattering from particles pumped through an optical aperture. It counts the number of particles whose diameters exceed six thresholds—0.1, 0.2, 0.3, 0.5, 1.0, and 5.0×10^{-6} m which we aggregate into the three size bins in the synthesis dataset.

31) *Aerosol number with diameter* $0.3 < D < 1.0 \times 10^{-6}$ m (number cm^{-3}). Aerosol measured at the surface by the LASAIR II-110 particle counter with diameter greater than 0.3×10^{-6} m and less than 1.0×10^{-6} m.

32) *Aerosol number with diameter* $> 1.0 \times 10^{-6}$ m (number cm^{-3}). Aerosol measured at the surface with diameter greater than 1.0×10^{-6} m.

33) *Water vapor path* (cm liquid equivalent). Integrated water vapor from two-channel upward-looking

microwave radiometers. A statistical retrieval is used to convert brightness temperature to integrated water vapor for the tropical atmosphere.

34) *Specific humidity* ($g \, kg^{-1}$). Surface specific humidity computed from the relative humidity and temperature from Vaisala HMP-300 series temperature/humidity sensor maintained by PSD on the forward mast, at a height of 18 m above sea level. The sensor is housed in an aspirated radiation shield.

35) *Lifting condensation level temperature* (K). Temperature of water condensation for an adiabatically lifted surface air parcel. Temperature and humidity of the surface parcel are measured by the sensors on the forward mast.

36) *Lifting condensation level height* (m). Height of condensation level for an adiabatically lifted surface air parcel.

37) *Total number of accumulation mode aerosols* (number cm^{-3}). Number of aerosols with a diameter greater than 0.1×10^{-6} m. This number was measured and provided to us by Texas A&M University in 2003 and 2004. In 2005–07, the number is computed as the sum of aerosols counted by the LASAIR II. Sensitivity of the instrument decreases slowly between cleaning and calibrating the instrument, affecting the absolute accuracy, yet we expect it to detect relative changes in the size-resolved drop concentrations reasonably well.

38) *Relative humidity* (%). Relative humidity as a percent of saturation humidity from the Vaisala HMP-300 probe on the mast at 14.8 m. Instrument accuracy is ±1.7% RH.

39) *Surface air pressure* (hPa). Atmospheric pressure on the deck of the ship measured in a static barometer housing at approximately 7 m above sea level. Available only in 2007 and 2008. Accurate to ±0.2 hPa.

f. *Rawinsonde observations*

GPS rawinsondes were released from the fantail of the ship, every 6 h (4 times daily) during normal cruise operation and every 4 h (6 times daily) when the ship was at mooring stations at 20°S, 75° and 85°W. Digital (RS92-SGP) rawinsondes have an accuracy of 0.2°C and 2% relative humidity in the troposphere, with response times under 0.5 s, and 0.2 m s^{-1} wind speed accuracy. Analog RS90 and RS80 rawinsondes used before 2004 have similar accuracy. Rawinsondes sample the atmosphere every 1 s with an ascent rate of approximately 5 m s^{-1}, yielding nearly 5-m vertical resolution. Data are subsequently averaged to the standard 10-m height or 1.0-hPa pressure increments and are made available for download in netCDF files.

REFERENCES

Angevine, W. M., A. B. White, and S. K. Avery, 1994: Boundary-layer depth and entrainment zone characterization with a boundary-layer profiler. *Bound.-Layer Meteor.,* **68,** 375–385.

Bianco, L., and J. M. Wilczak, 2002: Convective boundary layer depth: Improved measurement by Doppler radar wind profiler using fuzzy logic methods. *J. Atmos. Oceanic Technol.,* **19,** 1745–1758.

Bretherton, C. S., and Coauthors, 2004: The EPIC 2001 stratocumulus study. *Bull. Amer. Meteor. Soc.,* **85,** 967–977.

Cai, W., H. H. Hendon, and G. Meyers, 2005: Indian Ocean dipolelike variability in the CSIRO Mark 3 coupled climate model. *J. Climate,* **18,** 1449–1468.

Colbo, K., and R. Weller, 2007: The variability and heat budget of the upper ocean under the Chile-Peru stratus. *J. Mar. Res.,* **65,** 607–637.

Collins, W. D., and Coauthors, 2006: The Community Climate System Model version 3 (CCSM3). *J. Climate,* **19,** 2122–2143.

Comstock, K. K., C. S. Bretherton, and S. E. Yuter, 2005: Mesoscale variability and drizzle in southeast Pacific stratocumulus. *J. Atmos. Sci.,* **62,** 3792–3807.

Delworth, T. L., and Coauthors, 2006: GFDL's CM2 global coupled climate models. Part I: Formulation and simulation characteristics. *J. Climate,* **19,** 643–674.

de Szoeke, S. P., and S.-P. Xie, 2008: The tropical eastern Pacific seasonal cycle: Assessment of errors and mechanisms in IPCC AR4 coupled ocean–atmosphere general circulation models. *J. Climate,* **21,** 2573–2590.

——, Y. Wang, S.-P. Xie, and T. Miyama, 2006: Effect of shallow cumulus convection on the eastern Pacific climate in a coupled model. *Geophys. Res. Lett.,* **33,** L17713, doi:10.1029/2006GL026715.

Diansky, N. A., and E. M. Volodin, 2002: Simulation of present-day climate with a coupled atmosphere-ocean general circulation model. *Izv. Atmos. Oceanic Phys.,* **38,** 732–747.

Dong, X. Q., T. P. Ackerman, and E. E. Clothiaux, 1998: Parameterizations of the microphysical and shortwave radiative properties of boundary layer stratus from ground-based measurements. *J. Geophys. Res.,* **103,** 31 681–31 693.

Edson, J. B., A. A. Hinton, K. E. Prada, J. E. Hare, and C. W. Fairall, 1998: Direct covariance flux estimates from mobile platforms at sea. *J. Atmos. Oceanic Technol.,* **15,** 547–562.

Fairall, C. W., E. F. Bradley, J. S. Godfrey, G. A. Wick, J. B. Edson, and G. S. Young, 1996: Cool-skin and warm-layer effects on sea surface temperature. *J. Geophys. Res.,* **101,** 1295–1308.

——, A. B. White, J. B. Edson, and J. E. Hare, 1997: Integrated shipboard measurements of the marine boundary layer. *J. Atmos. Oceanic Technol.,* **14,** 338–359.

——, P. O. G. Persson, E. F. Bradley, R. E. Payne, and S. P. Anderson, 1998: A new look at calibration and use of Eppley precision infrared radiometers. Part I: Theory and application. *J. Atmos. Oceanic Technol.,* **15,** 1229–1242.

——, E. F. Bradley, J. E. Hare, A. A. Grachev, and J. B. Edson, 2003: Bulk parameterization of air–sea fluxes: Updates and verification for the COARE algorithm. *J. Climate,* **16,** 571–591.

——, T. Uttal, D. Hazen, J. Hare, M. F. Cronin, N. Bond, and D. E. Veron, 2008: Observations of cloud, radiation, and surface forcing in the equatorial eastern Pacific. *J. Climate,* **21,** 655–673.

Flato, G. M., and G. J. Boer, 2001: Warming asymmetry in climate change simulations. *Geophys. Res. Lett.,* **28,** 195–198.

Goosse, H., and T. Fichefet, 1999: Importance of ice-ocean interactions for the global ocean circulation: A model study. *J. Geophys. Res.,* **104,** 337–355.

Gordon, C., and Coauthors, 2000a: The simulation of SST, sea ice extents and ocean heat transports in a version of the Hadley Centre coupled model without flux adjustments. *Climate Dyn.,* **16,** 147–168.

——, A. Rosati, and R. Gudgel, 2000b: Tropical sensitivity of a coupled model to specified ISCCP low clouds. *J. Climate,* **13,** 2239–2260.

Halpern, D., 1974: Observations of the deepening of the wind-mixed layer in the northeast Pacific Ocean. *J. Phys. Oceanogr.,* **4,** 454–466.

Han, Y., and E. R. Westwater, 2000: Analysis and improvement of tipping calibration for ground-based microwave radiometers. *IEEE Trans. Geosci. Remote Sens.,* **38,** 1260–1276.

Iqbal, M., 1988: Spectral and total sun radiance under cloudless skies. *Physical Climatology for Solar and Wind Energy,* R. Guzzi and C. G. Justus, Eds., World Scientific, 196–242.

Jiang, C., M. F. Cronin, K. A. Kelly, and L. Thompson, 2005: Evaluation of a hybrid satellite- and NWP-based turbulent heat flux product using Tropical Atmosphere-Ocean (TAO) buoys. *J. Geophys. Res.,* **110,** C09007, doi:10.1029/2004JC002824.

Jungclaus, J. H., and Coauthors, 2006: Ocean circulation and tropical variability in the coupled model ECHAM5/MPI-OM. *J. Climate,* **19,** 3771–3791.

Large, W. G., and S. G. Yeager, 2008: The global climatology of an interannually varying air–sea flux data set. *Climate Dyn.,* 341–364, doi:10.1007/s00382-008-0441-3.

Ma, C.-C., C. R. Mechoso, A. W. Robertson, and A. Arakawa, 1996: Peruvian stratus clouds and the tropical Pacific circulation: A coupled ocean–atmosphere GCM study. *J. Climate,* **9,** 1635–1645.

Mechoso, C. R., and Coauthors, 1995: The seasonal cycle over the tropical Pacific in coupled ocean–atmosphere general circulation models. *Mon. Wea. Rev.,* **123,** 2825–2838.

Meehl, G. A., W. M. Washington, W. D. Collins, J. M. Arblaster, A. Hu, L. E. Buja, W. G. Strand, and H. Teng, 2005: How much more global warming and sea level rise? *Science,* **307,** 1769–1772.

——, T. Delworth, R. J. Stouffer, M. Latif, B. McAvaney, and J. F. B. Mitchell, 2007: The WCRP CMIP3 multimodel dataset: A new era in climate change research. *Bull. Amer. Meteor. Soc.,* **88,** 1383–1394.

Nozawa, T., T. Nagashima, H. Shiogama, and S. A. Crooks, 2005: Detecting natural influence on surface air temperature change in the early twentieth century. *Geophys. Res. Lett.,* **32,** L20719, doi:10.1029/2005GL023540.

Platnick, S., M. D. King, S. A. Ackerman, W. P. Menzel, B. A. Baum, J. C. Riedi, and R. A. Frey, 2003: The MODIS cloud products: Algorithms and examples from Terra. *IEEE Trans. Geosci. Remote Sens.,* **41,** 459–473.

Reynolds, R. W., and T. M. Smith, 1995: A high-resolution global sea surface temperature climatology. *J. Climate,* **8,** 1571–1583.

Risien, C. M., and D. B. Chelton, 2008: A global climatology of surface wind and wind stress fields from eight years of QuikSCAT scatterometer data. *J. Phys. Oceanogr.,* **38,** 2379–2413.

Salas-Mélia, D., and Coauthors, 2005: Description and validation of CNRM-CM3 global coupled climate model. Note de centre GMGEC, CNRM 103, 36 pp.

Siebesma, A. P., and Coauthors, 2004: Cloud representation in general-circulation models over the northern Pacific Ocean: A EUROCS intercomparison study. *Quart. J. Roy. Meteor. Soc.,* **130,** 3245–3267, doi:10.1256/qj.03.146.

Stephens, G. L., S. Ackerman, and E. A. Smith, 1984: A shortwave parameterization revised to improve cloud absorption. *J. Atmos. Sci.,* **41,** 687–690.

Stokes, G. M., and S. E. Schwartz, 1994: The Atmospheric Radiation Measurement (ARM) Program: Programmatic background and design of the cloud and radiation test bed. *Bull. Amer. Meteor. Soc.,* **75,** 1201–1221.

Toniazzo, T., C. R. Mechoso, L. C. Shaffrey, and J. M. Slingo, 2010: Upper-ocean heat budget and ocean eddy transport in the south-east Pacific in a high-resolution coupled model. *Climate Dyn.,* in press, doi:10.1007/s00382-009-0703-8.

Westwater, E. R., Y. Han, M. D. Shupe, and S. Y. Matrosov, 2001: Analysis of integrated cloud liquid and precipitable water vapor retrievals from microwave radiometers during the Surface Heat Budget of the Arctic Ocean project. *J. Geophys. Res.,* **106,** 32 019–32 030.

Wood, R., C. R. Mechoso, C. S. Bretherton, B. Huebert, and R. Weller, 2007: The VAMOS Ocean-Cloud-Atmosphere-Land Study (VOCALS). *U.S. CLIVAR Variations,* Vol. 5, No. 1, U.S. CLIVAR Program Office, Washington, DC, 1–16.

Xie, S. P., and Coauthors, 2007: A regional ocean–atmosphere model for eastern Pacific climate: Toward reducing tropical biases. *J. Climate,* **20,** 1504–1522.

Yu, J.-Y., and C. R. Mechoso, 1999a: A discussion on the errors in the surface heat fluxes simulated by a coupled GCM. *J. Climate,* **12,** 416–426.

——, and ——, 1999b: Links between annual variations of Peruvian stratocumulus clouds and of SST in the eastern equatorial Pacific. *J. Climate,* **12,** 3305–3318.

Yu, L., and R. Weller, 2007: Objectively analyzed air–sea heat fluxes for the global ice-free oceans (1981–2005). *Bull. Amer. Meteor. Soc.,* **88,** 527–539.

Yu, Y. Q., X. H. Zhang, and Y. F. Guo, 2004: Global coupled ocean-atmosphere general circulation models in LASG/IAP. *Adv. Atmos. Sci.,* **21,** 444–455.

Yukimoto, S., and Coauthors, 2001: The New Meteorological Research Institute Coupled GCM (MRI-CGCM2)—Model climate and variability. *Pap. Meteor. Geophys.,* **51,** 47–88.

Zhang, Y., W. B. Rossow, A. A. Lacis, V. Oinas, and M. I. Mishchenko, 2004: Calculation of radiative fluxes from the surface to top of atmosphere based on ISCCP and other global data sets: Refinements of the radiative transfer model and the input data. *J. Geophys. Res.,* **109,** D19105, doi:10.1029/2003JD004457.

Zheng, Y., T. Shinoda, G. N. Kiladis, J. Lin, E. J. Metzger, H. E. Hurlburt, and B. S. Giese, 2010: Upper-ocean processes under the stratus cloud deck in the southeast Pacific Ocean. *J. Phys. Oceanogr.,* **40,** 103–120.

Zuidema, P., E. R. Westwater, C. Fairall, and D. Hazen, 2005: Ship-based liquid water path estimates in marine stratocumulus. *J. Geophys. Res.,* **110,** D20206, doi:10.1029/2005jd005833.